$I = 1/2$ S-wave and P-wave $K\pi$ scattering and the κ and K^* resonances from lattice QCD

Gumaro Rendon,[1,*] Luka Leskovec,[2,3] Stefan Meinel,[4] John Negele,[5] Srijit Paul,[6] Marcus Petschlies,[7] Andrew Pochinsky,[5] Giorgio Silvi,[8] and Sergey Syritsyn[9,10]

[1]*Department of Physics, Brookhaven National Laboratory, Upton, New York 11973, USA*
[2]*Thomas Jefferson National Accelerator Facility, Newport News, Virginia 23606, USA*
[3]*Department of Physics, Old Dominion University, Norfolk, Virginia 23529, USA*
[4]*Department of Physics, University of Arizona, Tucson, Arizona 85721, USA*
[5]*Center for Theoretical Physics, Laboratory for Nuclear Science and Department of Physics, Massachusetts Institute of Technology, Cambridge, Massachusetts 02139, USA*
[6]*Institut für Kernphysik, Johannes Gutenberg-Universität Mainz, 55099 Mainz, Germany*
[7]*Helmholtz-Institut für Strahlen-und Kernphysik, Rheinische Friedrich-Wilhelms-Universität Bonn, Nußallee 14-16, 53115 Bonn, Germany*
[8]*Forschungszentrum Jülich GmbH, Jülich Supercomputing Centre, 52425 Jülich, Germany*
[9]*Department of Physics and Astronomy, Stony Brook University, Stony Brook, New York 11794, USA*
[10]*RIKEN BNL Research Center, Brookhaven National Laboratory, Upton, New York 11973, USA*

(Received 18 July 2020; accepted 23 September 2020; published 28 December 2020)

We present a lattice-QCD determination of the elastic isospin-1/2 S-wave and P-wave $K\pi$ scattering amplitudes as a function of the center-of-mass energy using Lüscher's method. We perform global fits of K-matrix parametrizations to the finite-volume energy spectra for all irreducible representations with total momenta up to $\sqrt{3}\frac{2\pi}{L}$; this includes irreducible representations (irreps) that mix the S- and P-waves. Several different parametrizations for the energy dependence of the K-matrix are considered. We also determine the positions of the nearest poles in the scattering amplitudes, which correspond to the broad κ resonance in the S-wave and the narrow $K^*(892)$ resonance in the P-wave. Our calculations are performed with $2+1$ dynamical clover fermions for two different pion masses of 317.2(2.2) and 175.9(1.8) MeV. Our preferred S-wave parametrization is based on a conformal map and includes an Adler zero; for the P-wave, we use a standard pole parametrization including Blatt-Weisskopf barrier factors. The S-wave κ-resonance pole positions are found to be $[0.86(12) - 0.309(50)i]$ GeV at the heavier pion mass and $[0.499(55) - 0.379(66)i]$ GeV at the lighter pion mass. The P-wave K^*-resonance pole positions are found to be $[0.8951(64) - 0.00250(21)i]$ GeV at the heavier pion mass and $[0.8718(82) - 0.0130(11)i]$ GeV at the lighter pion mass, which corresponds to couplings of $g_{K^*K\pi} = 5.02(26)$ and $g_{K^*K\pi} = 4.99(22)$, respectively.

DOI: 10.1103/PhysRevD.102.114520

I. INTRODUCTION

As the simplest two-meson system with unequal mass and carrying strangeness, the $K\pi$ system plays an important role in particle and nuclear physics. A review of the early history of $K\pi$ scattering and the associated resonances can be found in Ref. [1]. The $K\pi$ system also occurs in heavy-meson weak decay processes that are used to search for physics beyond the Standard Model [2–6]. This includes multibody nonleptonic decays such as $B \to K\pi\pi$, in which large CP-violating effects have been observed and two-body resonant substructures are seen [7], and semileptonic decays such as $B \to K\pi\ell^+\ell^-$, which currently provide hints for new fundamental physics [8–15].

$K\pi$ scattering has been studied in fixed-target scattering experiments with charged-kaon beams [16,17] and, at low energies, through the formation and breakup of electromagnetically bound $K\pi$ atoms [18,19]. Further detailed investigations are planned using neutral kaon beams at the GlueX experiment [20].

The $I = 1/2$ S-wave scattering amplitude is observed to be elastic up to approximately 1.3 GeV [16,17]. The results for the elastic scattering phase shift slowly but monotonically increase and reach 60° at approximately 1.1 GeV. The rise in the phase shift is likely due to a very wide resonance, the κ [also referred to as $K_0^*(800)$ or, more recently, $K_0^*(700)$]. However, since the phase shift does not cross

*jrendonsu@bnl.gov

90°, the existence of the κ remains a topic of discussion [21]; the latest update of the Particle Data Group database [22] still lists the κ as "requires confirmation". Because the κ is such a wide resonance with total decay width $\Gamma_{\text{total}} \approx 600$ MeV, its description is more involved. The search for a proper description and explanation for this elusive resonance is a hot topic in hadronic physics. The basic idea is to construct a parametrization of the scattering amplitude and fit it to the experimental data; by analytically continuing the amplitude into the complex plane, one searches for a pole attributed to the κ resonance. The experimental data [16,17] have been described by effective Lagrangians incorporating chiral symmetry [23–37] and models of meson interactions [38,39]. The κ was also studied in the large N_c limit of QCD [40,41] and with the inverse amplitude method [42,43]. The authors of Refs. [44,45] used Roy-Steiner equations to determine the pole of the κ resonance. Less rigorous but similar studies using dispersion relations [46,47] are able to consistently find the κ pole. The relations between chiral perturbation theory and dispersion relations were explored in Ref. [48]. Fits of various models [49] and Padé approximants [50] to the experimental data led to similar results. Furthermore, it was observed that a κ resonance is necessary to explain an enhancement [51,52] in other production channels in the experiments E791 [53] and BES [54,55].

In the P-wave, the $I = 1/2$ $K\pi$ scattering amplitude at energies below the $K\eta$ threshold is well described by a simple Breit-Wigner form with a single resonance, the $K^*(892)$,[1] as observed in various processes ranging from kaon beam experiments to τ decays and D-meson decays [22]. The total decay width of the $K^*(892)$ is approximately 50.8(0.9) MeV [22] with branching ratios to $K\pi$ being 99.9%, to $K\gamma$ at the order of 10^{-3}, and less than 10^{-5} to $K\pi\pi$.

In lattice QCD, scattering amplitudes can be determined from finite-volume energy spectra using Lüscher's method [56–65]. For S-wave $K\pi$ scattering, the early lattice QCD calculations focused on scattering lengths describing low-energy scattering. The first such calculation, published in 2004, was performed for $I = 3/2$ only and in the quenched approximation [66]. This was followed by a calculation in 2006 that included $N_f = 2 + 1$ staggered sea quarks but employed a domain-wall valence action [67]; the authors determined the $I = 3/2$ S-wave scattering length directly from the lattice and used chiral symmetry to extract also the $I = 1/2$ scattering length at several pion masses. The S-wave scattering lengths have also been determined from scalar form factors for semileptonic decays [68]. Reference [69] contains the first direct lattice QCD calculation of the S-wave scattering length for both $I = 1/2$ and $I = 3/2$, albeit in the quenched approximation. The $K\pi$ system was also investigated using a staggered action for both the valence and sea quarks in Refs. [70–73]. Note that the presence of extra nondegenerate fermion tastes when using a staggered action introduces complications for the Lüscher method that are not yet fully understood. More recent dynamic lattice QCD calculations of $K\pi S$-wave the scattering lengths employed valence Wilson fermions with either $N_f = 2$ [74], $N_f = 2 + 1$ [75] or $N_f = 2 + 1 + 1$ [76] dynamical Wilson fermions.

Early attempts to investigate the κ resonance on the lattice focused on the energy spectrum and involved searching for additional energy levels that could be associated with the resonance. Finite-volume energies were investigated for the κ system in Refs. [77] and [78]. In the latter reference, the quark-disconnected contributions were neglected. The authors later found that this leads to the wrong spectrum [74], as also discussed in Ref. [79] from a perturbative point of view. In the early 2010s, it became clear that the κ does not behave like the typical resonance on the lattice. Using unitarized chiral perturbation theory models, Refs. [80–85] determined the finite-volume energies and investigated what can be expected in lattice QCD calculations.

To date, there have been few fully fledged determinations of the energy dependence of $K\pi$ scattering amplitudes with dynamical lattice QCD. The first such studies focused on the P-wave in the K^* resonance region. In Ref. [86], $N_f = 2 + 1$ staggered quarks were used to determine the K^* phase shift from the rest frame spectra. A similar calculation with $N_f = 2$ Wilson quarks included also moving frames [87] and determined the scattering phase shift and the K^* width. The authors of Ref. [88] repeated the calculation for the ρ and the K^* at an almost physical pion mass on two large $N_f = 2$ gauge ensembles. A more comprehensive study was published in Refs. [89,90], where the authors calculated the scattering amplitudes in S-, P-, and D-waves with $I = 1/2$ and $I = 3/2$ and determined their resonance content. They employed anisotropic gauge ensembles with $N_f = 2 + 1$ Wilson fermions, similarly to Ref. [91]. Recently, Ref. [92] reported a calculation of $I = 1/2$ S- and P-wave scattering amplitudes at an unprecedented number of quark masses.

In the following, we present a new detailed analysis of $I = 1/2$ $K\pi$ scattering using lattice QCD. This work provides further information on the interactions and resonances in this system and also constitutes our first step toward a future lattice calculation of semileptonic form factors with $K\pi$ final states based on the formalism developed in Ref. [93]. We simultaneously determine the energy dependence of both the S-wave and P-wave scattering amplitudes below the $K\eta$ threshold and investigate several different parametrizations with and without an Adler zero for the S-wave amplitude. We determine the pole locations corresponding to the κ and K^* resonances

[1]In the remainder of the text, we will denote the $K^*(892)$ in short as K^*.

and also present the $K^*K\pi$ couplings. Our calculation is performed on two different gauge-field ensembles with $N_f = 2 + 1$ dynamical clover fermions; the first has a lattice size of $32^3 \times 96$ with a spacing of $a \approx 0.114$ fm and a pion mass of $m_\pi \approx 317$ MeV, while the second has a lattice size of $48^3 \times 96$ with $a \approx 0.088$ fm and $m_\pi \approx 176$ MeV.

The paper is organized as follows. We begin by overviewing the continuum description of elastic $K\pi$ scattering in Sec. II. In Sec. III, we briefly describe the lattice gauge-field ensembles, while Sec. IV gives details on the construction of the interpolating operators and correlation matrices. Our spectrum results are shown in Sec. V, and the finite-volume methods for the determination of the scattering amplitudes are discussed in Sec. VI. We present our results for the energy dependence of the phase shifts and the pole locations in Sec. VII. Our conclusions, including a comparison with previous work, are given in Sec. VIII.

II. PARAMETRIZATIONS OF THE SCATTERING AMPLITUDES

In this section, we briefly review the K-matrix formalism describing $2 \to 2$ scattering [94] and then discuss the specific parametrizations we use to describe $K\pi$ scattering with $I(J^P) = 1/2(0^+)$ and $I(J^P) = 1/2(1^-)$. In general, the multichannel scattering matrix can be expressed as

$$S^{(\ell)}(s) = 1 + 2iT^{(\ell)}(s), \tag{1}$$

where $T^{(\ell)}$ is the T-matrix (also known as the scattering amplitude), which depends on the invariant mass s of the system, and ℓ is the partial wave of the scattering process. From the unitarity of $S^{(\ell)}$, one gets

$$\frac{1}{2i}[T^{(\ell)}_{ij} - T^{(\ell)*}_{ji}] = \mathrm{Im}T^{(\ell)}_{ij} = \sum_k T^{(\ell)*}_{ik}\theta(s - s^{(k)}_{\mathrm{thr}})T^{(\ell)}_{kj}, \tag{2}$$

where we used that, due to time-reversal invariance of the strong interaction, the T-matrix is symmetric. Here, the indices $i, j, \ldots$ label the scattering channels, and $s^{(i)}_{\mathrm{thr}}$ denotes the threshold in channel i. Equivalently,

$$\mathrm{Im}\{T^{(\ell)-1}\}_{ij} = -\theta(s - s^{(i)}_{\mathrm{thr}})\delta_{ij}. \tag{3}$$

That means that we can split the real and imaginary contributions to $T^{(\ell)-1}$ in the following way,

$$\{T^{(\ell)-1}\}_{ij} = \{K^{(\ell)-1}\}_{ij} - i\theta(s - s^{(i)}_{\mathrm{thr}})\delta_{ij}, \tag{4}$$

where $K^{(\ell)}$ has to be real and symmetric to ensure unitarity and time-reversal invariance.

In order to incorporate the correct analytic structure from the $K\pi$ threshold, we define the phase-space factor ρ, which is a diagonal matrix in channel space:

$$\rho_{ii} = \sqrt{\left(1 - \left(\frac{m_a^i + m_b^i}{\sqrt{s}}\right)^2\right)\left(1 - \left(\frac{m_a^i - m_b^i}{\sqrt{s}}\right)^2\right)}. \tag{5}$$

Above, a and b label the two mesons undergoing elastic scattering in channel i. For example, at scattering energies above the $K\eta$ threshold we have two scattering channels, $i = 0, 1$, which correspond to the scattering of $K\pi$ and $K\eta$, respectively. However, the $K\eta$ channel is not relevant at the energies we consider here, and our spectra can be described by purely elastic $K\pi$ scattering ($i = 0$ only). We omit the channel indices in the remainder of the paper.

Using the phase-space factor, we define the rescaled K-matrix $\hat{K}^{(\ell)}$ through

$$K^{(\ell)} = \rho^{1/2}\hat{K}^{(\ell)}\rho^{1/2}. \tag{6}$$

The elastic scattering phase shift δ_ℓ is related to the scattering amplitude as

$$T^{(\ell)} = e^{i\delta_\ell}\sin(\delta_\ell) = \frac{1}{\cot\delta_\ell - i} \tag{7}$$

and to the K-matrix as

$$K^{(\ell)} = \tan(\delta_\ell) \quad \text{and} \quad \hat{K}^{(\ell)} = \frac{1}{\rho}\tan(\delta_\ell). \tag{8}$$

We now proceed to the discussion of the parametrizations we use for the s dependence. For the P-wave, which is governed by the narrow K^* resonance, we find that a simple one-pole K-matrix parametrization with Blatt-Weisskopf barrier factors describes the data well. For the S-wave, we also consider three additional parametrizations: the effective-range expansion [95,96], Bugg's parametrization [97,98] that accounts for a zero in the scattering amplitude known as the Adler zero [99–101], and the conformal-map-based parametrization used in Ref. [50], which also has an Adler zero.

A. Chung's parametrization

Chung's parametrization is a raw K-matrix pole parametrization [94] combined with Blatt-Weisskopf barrier factors [102]. The latter describe a centrifugal barrier effect in the P-wave but is trivial for S-wave scattering. For both the S- and P-waves, the K-matrix pole parametrization is

$$\hat{K}^{(\ell)} = \sum_\alpha \frac{g_{\ell,\alpha}(\sqrt{s})g_{\ell,\alpha}(\sqrt{s})}{(m^2_{\ell,\alpha} - s)\rho}, \tag{9}$$

where α labels the resonances present and

$$g_{\ell,\alpha}(\sqrt{s}) = \sqrt{m_{\ell,\alpha}\Gamma_{\ell,\alpha}(\sqrt{s})} \tag{10}$$

with

$$\Gamma_{\ell,\alpha}(\sqrt{s}) = \gamma^2_{\ell,\alpha}\,\rho[B^\ell_\alpha(k,k_\alpha)]^2\Gamma^0_{\ell,\alpha}. \tag{11}$$

Here, the $\gamma_{\ell,\alpha}$ are the resonance couplings, $B^\ell_\alpha(k,k_\alpha)$ are the Blatt-Weisskopf barrier factors (defined further below), and the parameters $\Gamma^0_{\ell,\alpha}$ are related to the widths of the resonances. Since only the product $\gamma^2_{\ell,\alpha}\Gamma^0_{\ell,\alpha}$ appears in $\Gamma_{\ell,\alpha}(\sqrt{s})$, we perform our fits in terms of new parameters $g^0_{\ell,\alpha}$ defined as

$$g^0_{\ell,\alpha} = \gamma_{\ell,\alpha}\sqrt{m_{\ell,\alpha}\Gamma^0_{\ell,\alpha}}. \tag{12}$$

Inserting Eq. (12) into Eq. (9) gives the final form

$$\hat{K}^{(\ell)} = \sum_\alpha \frac{g^0_{\ell,\alpha}g^0_{\ell,\alpha}B^\ell_\alpha(k,k_\alpha)B^\ell_\alpha(k,k_\alpha)}{(m^2_{\ell,\alpha}-s)}. \tag{13}$$

The Blatt-Weisskopf factors are functions of k; the scattering momentum at the given s; and k_α, the scattering momentum at $s = m^2_\alpha$. The scattering momentum k is defined via

$$\sqrt{s} = \sqrt{m^2_\pi + k^2} + \sqrt{m^2_K + k^2}, \tag{14}$$

which gives

$$k^2 = \frac{s^2 + (m^2_\pi - m^2_K)^2 - 2s(m^2_\pi + m^2_K)}{4s}. \tag{15}$$

The Blatt-Weisskopf factors are equal to $B^\ell_\alpha(k,k_\alpha) = F_\ell(k)/F_\ell(k_\alpha)$, where

$$F_0(k) = 1, \tag{16}$$

$$F_1(k) = \sqrt{\frac{2(kR_{1,\alpha})^2}{1+(kR_{1,\alpha})^2}}, \tag{17}$$

with $R_{1,\alpha}$ the characteristic range for $\ell = 1$, which we also take to be a fit parameter. Since we include only one resonance in each partial wave, we omit the index α in the following and denote the fit parameters as

$$m_\ell, g^0_\ell \quad (\text{for } \ell = 0,1), R_1. \tag{18}$$

B. Effective-range expansion

The effective-range expansion (ERE) to order k^2 for $\ell = 0$ is given by [95,96]

$$\hat{K}^{(\ell=0)^{-1}} = \frac{\rho}{k}\left(\frac{1}{a} + \frac{1}{2}r_0k^2\right), \tag{19}$$

where a is the zero-energy scattering length and r_0 represents the effective range of the interaction. The actual fit parameters we use are

$$c_0 = \frac{1}{a}, \qquad c_1 = \frac{1}{2}r_0. \tag{20}$$

C. Bugg's parametrization

The author of Ref. [98] performed a fit to FOCUS and E791 data for the $D \to K\pi\pi$ decay [103,104], using a modified version of the parametrization of Ref. [31] to accommodate the broad nature of the κ resonance. This is a K-matrix pole parametrization where the width is taken to have a zero of the form $s - s_A$, intended to account for the prediction from chiral perturbation theory that the T-matrix has a zero at $s = s_A$ (the Adler zero), where [50]

$$s_A = \frac{1}{5}\left(m^2_K + m^2_\pi + 2\sqrt{4(m^2_K - m^2_\pi)^2 + m^2_K m^2_\pi}\right). \tag{21}$$

The parametrization enables the scattering amplitude to reproduce the experimental phase shift near the threshold much better. A model explanation for this form of the amplitude is discussed in Ref. [39]. We implement this parametrization by multiplying the K-matrix pole with an enveloping term of the form $s - s_A$ so that the T-matrix also becomes zero as predicted:

$$\hat{K}^{(\ell=0)} = \frac{[G_0(s)]^2}{m^2_0 - s}, \tag{22}$$

$$G_0(s) = G^0_0\sqrt{\frac{s - s_A}{s_A - m^2_0}}. \tag{23}$$

D. Conformal map parametrization

The final parametrization we consider for the S-wave is that of Ref. [50], which involves a power series in a new variable $\omega(s)$. The regions of analyticity in the complex-s plane are conformally mapped to the interior of the unit disk, while the elastic, inelastic, left-hand, and circular cuts are mapped to the circle $|\omega| = 1$. The parametrization also includes an Adler zero and is given by

$$K^{(\ell=0)-1} = \frac{\sqrt{s}}{2k}F(s)\sum_n B_n\omega^n(s) \tag{24}$$

with

$$F(s) = \frac{1}{s - s_A}. \tag{25}$$

The conformal map is defined as

$$\omega(y) = \frac{\sqrt{y} - \alpha\sqrt{y_0 - y}}{\sqrt{y} + \alpha\sqrt{y_0 - y}}, \qquad y(s) = \left(\frac{s - \Delta_{K\pi}}{s + \Delta_{K\pi}}\right)^2, \quad (26)$$

where $\Delta_{K\pi} = m_K^2 - m_\pi^2$ and $y_0 \equiv y(s_0)$. The constant s_0 determines the maximum value of s for which the map is applicable, while the constant α determines the origin of the expansion. We set $\sqrt{s_0}$ equal to the $K\eta$ threshold, using leading-order chiral perturbation theory to express m_η in terms of m_K and m_π:

$$\sqrt{s_0} = m_K + \sqrt{\frac{4m_K^2 - m_\pi^2}{3}}. \quad (27)$$

We choose $\alpha = 1.3$ for both ensembles so that the origin of the expansion is around the middle of the data points. We found it sufficient to expand to first order in ω.

III. GAUGE ENSEMBLES AND SINGLE-MESON ENERGIES

In this work, we utilize two different gauge-field ensembles, labeled C13 and D6, with parameters given in Table I. These ensembles use the tadpole-improved tree-level Symanzik gluon action [105–108] and include $2 + 1$ flavors of clover fermions [109,110]. The gauge links in the fermion action are Stout smeared [111] with a staple weight of $\rho = 0.125$. We use the same clover action also for the valence quarks. The lattice spacings, a, were determined using the $\Upsilon(2S) - \Upsilon(1S)$ splitting [112,113] computed with improved lattice non-relativistic quantum chromodynamics [114].

When using Lüscher's method, the pion and kaon dispersion relations are needed to relate energies to scattering momenta. To study the dispersion relations on the lattice, we computed pion and kaon two-point correlation functions projected to different momenta. Fits of the dispersion relations on the D6 ensemble are shown in Figs. 1 and 2. We find that the data with $|\vec{p}| \leq \sqrt{3} \cdot 2\pi/L$ are consistent with the relativistic continuum dispersion relation on both ensembles, and we therefore use this form in the further analysis.

TABLE I. Parameters of the gauge-field ensembles.

Parameters	C13	D6
$N_s^3 \times N_t$	$32^3 \times 96$	$48^3 \times 96$
β	6.1	6.3
$am_{u,d}$	−0.285	−0.2416
am_s	−0.245	−0.205
c_{SW}	1.2493	1.2054
a (fm)	0.11403(77)	0.08766(79)
L (fm)	3.649(25)	4.208(38)
am_π	0.18332(29)	0.07816(35)
am_K	0.30475(17)	0.22803(15)
m_π (MeV)	317.2(2.2)	175.9(1.8)
m_K (MeV)	527.4(3.6)	513.3(4.6)
N_{config}	896	328

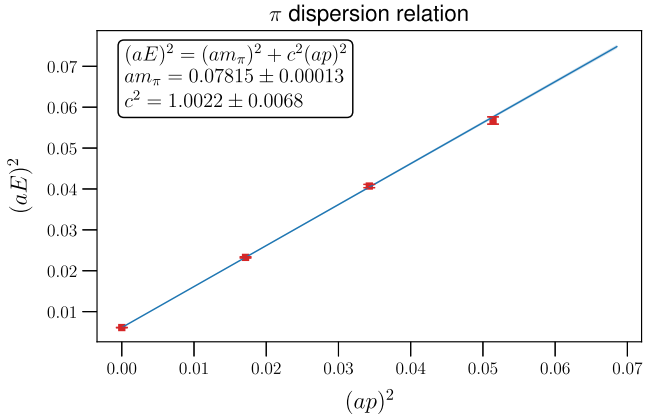

FIG. 1. Pion dispersion relation for D6 ensemble. The mass of the π and the speed of light determined from the multiple-momenta simultaneous fit matches the relativistic dispersion relation with the rest frame π mass fit.

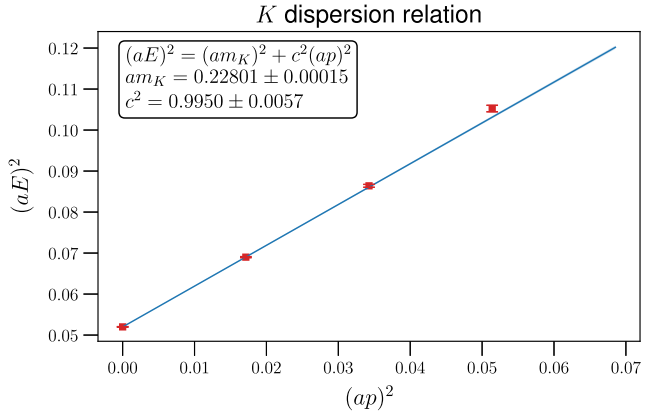

FIG. 2. Like Fig. 1, but for the kaon.

IV. INTERPOLATING OPERATORS AND CORRELATION MATRIX CONSTRUCTION

To determine the $K\pi$ scattering amplitudes, we use the Lüscher method; the first step of such a calculation is to determine the finite-volume spectra for different total momenta and irreducible representations. We determine the spectra in specific momentum frames and irreducible representations by calculating two-point correlation functions constructed from a set of interpolating operators.

A. Interpolating operators

We use two types of interpolating operators in this work. The single-hadron operators, built from local quark-antiquark bilinears, are constructed as follows:

$$K_i^{*+}(t,\vec{P}) = \sum_{\vec{x}} e^{i\vec{P}\cdot\vec{x}}\bar{s}(t,\vec{x})\gamma_i u(t,\vec{x}), \tag{28}$$

$$K_{ti}^{*+}(t,\vec{P}) = \sum_{\vec{x}} e^{i\vec{P}\cdot\vec{x}}\bar{s}(t,\vec{x})\gamma_t\gamma_i u(t,\vec{x}), \tag{29}$$

$$K_0^{+}(t,\vec{P}) = \sum_{\vec{x}} e^{i\vec{P}\cdot\vec{x}}\bar{s}(t,\vec{x}) u(t,\vec{x}). \tag{30}$$

These operators have manifest isospin $I = 1/2$; the projection to irreducible representations of the lattice symmetry group is discussed further below. The two-hadron operators are constructed from products of pseudoscalar π and K operators with definite individual momenta, combined to $I = 1/2$ via $SU(2)$ Clebsch-Gordan coefficients,

$$O_{K\pi}(t,\vec{p}_1,\vec{p}_2) = \sqrt{\frac{2}{3}}\pi^+(t,\vec{p}_1)K^0(t,\vec{p}_2) - \sqrt{\frac{1}{3}}\pi^0(t,\vec{p}_1)K^+(t,\vec{p}_2), \tag{31}$$

where

$$\pi^+(t,\vec{p}_1) = \sum_{\vec{x}} e^{i\vec{p}_1\cdot\vec{x}}\bar{d}(t,\vec{x})\gamma_5 u(t,\vec{x}), \tag{32}$$

$$\pi^0(t,\vec{p}_1) = \sum_{\vec{x}} e^{i\vec{p}_1\cdot\vec{x}}\frac{1}{\sqrt{2}}[\bar{d}(t,\vec{x})\gamma_5 d(t,\vec{x}) - \bar{u}(t,\vec{x})\gamma_5 u(t,\vec{x})], \tag{33}$$

$$K^+(t,\vec{p}_2) = \sum_{\vec{x}} e^{i\vec{p}_2\cdot\vec{x}}\bar{s}(t,\vec{x})\gamma_5 u(t,\vec{x}), \tag{34}$$

$$K^0(t,\vec{p}_2) = \sum_{\vec{x}} e^{i\vec{p}_2\cdot\vec{x}}\bar{s}(t,\vec{x})\gamma_5 d(t,\vec{x}). \tag{35}$$

All quark fields in the single-hadron and multihadron operators are Wuppertal smeared [115] with $\alpha_{\mathrm{Wup}} = 3.0$ and $N_{\mathrm{Wup}} = 20$ on the `C13` ensemble and $N_{\mathrm{Wup}} = 55$ on the `D6` ensemble, using APE-smeared gauge links [116] with $\alpha_{\mathrm{APE}} = 2.5$ and $N_{\mathrm{APE}} = 25$, 32 for `C13`, `D6` in the smearing kernel.

Since the finite-volume box in which we perform our calculation reduces the symmetry with respect to the infinite volume, we project the operators to the irreducible representations that respect the symmetry of the lattice:

$$O_{K\pi}^{\Lambda,\vec{P}} = \frac{\dim(\Lambda)}{\mathrm{order}(LG(\vec{P}))}\sum_{\vec{p}}\sum_{R\in LG(\vec{P})}\chi^{\Lambda}(R)O_{K\pi}(R\vec{p},\vec{P}-R\vec{p}), \tag{36}$$

$$O_{K^*,i}^{\Lambda,\vec{P}} = \frac{\dim(\Lambda)}{\mathrm{order}(LG(\vec{P}))}\sum_{R\in LG(\vec{P})}\chi^{\Lambda}(R)\sum_j R_{ij}K_j^{*+}(\vec{P}). \tag{37}$$

Above, $LG(\vec{P})$ denotes the Little Group on the lattice for total momentum $\vec{P}$ (i.e., the subgroup of the cubic group that remains a symmetry for the given momentum), and $\chi^{\Lambda}(R)$ are the characters for irrep Λ, which can be found for example in Ref. [117]. In the sum over $\vec{p}$ (with components being integer multiples of $2\pi/L$), we fix the magnitudes $|\vec{p}_1| = |R\vec{p}| = |\vec{p}|$ and $|\vec{p}_2| = |\vec{P} - R\vec{p}|$, and different choices for these magnitudes yield different operators in the same irrep.

In the following we will denote the irrep-projected operators as $O_A^{\Lambda,\vec{P}}$, where the operator index A counts the different internal structures within a given irrep, as detailed in Table II.

B. Wick contractions

The correlation matrix $C^{\Lambda,\vec{P}}(t)$ for irreducible representation Λ of Little Group $LG(\vec{P})$ is obtained from the interpolators defined above as

$$C_{AB}^{\Lambda,\vec{P}}(t_{\mathrm{snk}} - t_{\mathrm{src}}) = \langle O_A^{\Lambda,\vec{P}}(t_{\mathrm{snk}})O_B^{\Lambda,\vec{P}}(t_{\mathrm{src}})^{\dagger}\rangle, \tag{38}$$

where t_{src} is the source time and t_{snk} is the sink time. The correlation matrix elements are expressed in terms of quark propagators by performing the Wick contractions (i.e., by performing the path integral over the quark fields in a given gauge-field configuration). The resulting quark-flow diagrams are shown in Fig. 3 (for the case $I = 1/2$ considered here). The diagrams in Fig. 3 are obtained from point-to-all propagators (labeled f), sequential propagators (labeled seq), and stochastic time-slice-to-all propagators (labeled st), as in Ref. [118]. One summation over $\vec{x}$ at the source is eliminated using translational symmetry. In the following description of the different types of propagators, we omit the smearing kernels for brevity, but we note that all propagators are smeared at source and sink with the parameters given in Sec. IV A.

The point-to-all propagator for quark flavor q with full spin-color dilution is given by

$$S_{f_q}(t_{\mathrm{snk}},\vec{x}_{\mathrm{snk}};t_{\mathrm{src}},\vec{x}_{\mathrm{src}})_{\alpha\beta}^{ab} = \sum_{x,\beta',b'} D_q^{-1}(t_{\mathrm{snk}},\vec{x}_{\mathrm{snk}};x)_{\alpha,\beta'}^{a,b'}\eta^{(t_i,\vec{x}_{\mathrm{src}},\beta,b)}(x)_{\beta'}^{b'}, \tag{39}$$

where

$$\eta^{(t_i,\vec{x}_{\mathrm{src}},\beta,b)}(t,\vec{x})_{\beta'}^{b'} = \delta_{t,t_{\mathrm{src}}}\delta^{(3)}_{\vec{x},\vec{x}_{\mathrm{src}}}\delta_{b,b'}\delta_{\beta,\beta'}. \tag{40}$$

The sequential propagator S_{seq} follows from the solution of the lattice Dirac equation with right-hand side given by (39) restricted to the source time t_{src} and dressed with a vertex,

TABLE II. List of operators for all irreps that we use. The operators with structures labeled K_0^+, K_i^{*+}, and K_{ti}^{*+} are quark-antiquark operators, while the operators with structures labeled $K\pi$ are two-meson operators.

$\frac{L}{2\pi}\vec{P}$	Little group LG	Irrep Λ	Angular momentum content	Operator number	Operator structure
(0,0,0)	O_h	A_{1g}	$J = 0, 4, \ldots$	1	K_0^+
				2	$K\pi$ with $\lvert\vec{p}_1\rvert = \lvert\vec{p}_2\rvert = 0$
				3	$K\pi$ with $\lvert\vec{p}_1\rvert = \lvert\vec{p}_2\rvert = \frac{2\pi}{L}$
				4	$K\pi$ with $\lvert\vec{p}_1\rvert = \lvert\vec{p}_2\rvert = \sqrt{2}\frac{2\pi}{L}$
				5	$K\pi$ with $\lvert\vec{p}_1\rvert = \lvert\vec{p}_2\rvert = \sqrt{3}\frac{2\pi}{L}$
(0,0,0)	O_h	T_{1u}	$J = 1, 3, \ldots$	1	K_i^{*+}
				2	K_{ti}^{*+}
				3	$K\pi$ with $\lvert\vec{p}_1\rvert = \lvert\vec{p}_2\rvert = \frac{2\pi}{L}$
				4	$K\pi$ with $\lvert\vec{p}_1\rvert = \lvert\vec{p}_2\rvert = \sqrt{2}\frac{2\pi}{L}$
				5	$K\pi$ with $\lvert\vec{p}_1\rvert = \lvert\vec{p}_2\rvert = \sqrt{3}\frac{2\pi}{L}$
(0,0,1)	C_{4v}	A_1	$J = 0, 1, \ldots$	1	K_i^{*+}
				2	K_{ti}^{*+}
				3	K_0^+
				4	$K\pi$ with $\lvert\vec{p}_1\rvert = 0$ and $\lvert\vec{p}_2\rvert = \frac{2\pi}{L}$
				5	$K\pi$ with $\lvert\vec{p}_1\rvert = \frac{2\pi}{L}$ and $\lvert\vec{p}_2\rvert = 0$
				6	$K\pi$ with $\lvert\vec{p}_1\rvert = \frac{2\pi}{L}$ and $\lvert\vec{p}_2\rvert = \sqrt{2}\frac{2\pi}{L}$
				7	$K\pi$ with $\lvert\vec{p}_1\rvert = \sqrt{2}\frac{2\pi}{L}$ and $\lvert\vec{p}_2\rvert = \frac{2\pi}{L}$
				8	$K\pi$ with $\lvert\vec{p}_1\rvert = \sqrt{2}\frac{2\pi}{L}$ and $\lvert\vec{p}_2\rvert = \sqrt{3}\frac{2\pi}{L}$
				9	$K\pi$ with $\lvert\vec{p}_1\rvert = \sqrt{3}\frac{2\pi}{L}$ and $\lvert\vec{p}_2\rvert = \sqrt{2}\frac{2\pi}{L}$
(0,0,1)	C_{4v}	E	$J = 1, 2, \ldots$	1	K_i^{*+}
				2	K_{ti}^{*+}
				3	$K\pi$ with $\lvert\vec{p}_1\rvert = \sqrt{2}\frac{2\pi}{L}$ and $\lvert\vec{p}_2\rvert = \frac{2\pi}{L}$
				4	$K\pi$ with $\lvert\vec{p}_1\rvert = \frac{2\pi}{L}$ and $\lvert\vec{p}_2\rvert = \sqrt{2}\frac{2\pi}{L}$
				5	$K\pi$ with $\lvert\vec{p}_1\rvert = \sqrt{3}\frac{2\pi}{L}$ and $\lvert\vec{p}_2\rvert = \sqrt{2}\frac{2\pi}{L}$
				6	$K\pi$ with $\lvert\vec{p}_1\rvert = \sqrt{2}\frac{2\pi}{L}$ and $\lvert\vec{p}_2\rvert = \sqrt{3}\frac{2\pi}{L}$
(0,1,1)	C_{2v}	A_1	$J = 0, 1, \ldots$	1	K_i^{*+}
				2	K_{ti}^{*+}
				3	K_0^+
				4	$K\pi$ with $\lvert\vec{p}_1\rvert = 0$ and $\lvert\vec{p}_2\rvert = \sqrt{2}\frac{2\pi}{L}$
				5	$K\pi$ with $\lvert\vec{p}_1\rvert = \sqrt{2}\frac{2\pi}{L}$ and $\lvert\vec{p}_2\rvert = 0$
				6	$K\pi$ with $\lvert\vec{p}_1\rvert = \frac{2\pi}{L}$ and $\lvert\vec{p}_2\rvert = \sqrt{3}\frac{2\pi}{L}$
				7	$K\pi$ with $\lvert\vec{p}_1\rvert = \lvert\vec{p}_2\rvert = \frac{2\pi}{L}$
				8	$K\pi$ with $\lvert\vec{p}_1\rvert = \sqrt{3}\frac{2\pi}{L}$ and $\lvert\vec{p}_2\rvert = \frac{2\pi}{L}$
				9	$K\pi$ with $\lvert\vec{p}_1\rvert = \lvert\vec{p}_2\rvert = \sqrt{2}\frac{2\pi}{L}$
(0,1,1)	C_{2v}	B_1	$J = 1, 2, \ldots$	1	K_i^{*+}
				2	K_{ti}^{*+}
				3	$K\pi$ with $\lvert\vec{p}_1\rvert = \sqrt{3}\frac{2\pi}{L}$ and $\lvert\vec{p}_2\rvert = \frac{2\pi}{L}$
				4	$K\pi$ with $\lvert\vec{p}_1\rvert = \lvert\vec{p}_2\rvert = \sqrt{2}\frac{2\pi}{L}$
				5	$K\pi$ with $\lvert\vec{p}_1\rvert = \frac{2\pi}{L}$ and $\lvert\vec{p}_2\rvert = \sqrt{3}\frac{2\pi}{L}$
(0,1,1)	C_{2v}	B_2	$J = 1, 2, \ldots$	1	K_i^{*+}
				2	K_{ti}^{*+}
				3	$K\pi$ with $\lvert\vec{p}_1\rvert = \lvert\vec{p}_2\rvert = \frac{2\pi}{L}$
				4	$K\pi$ with $\lvert\vec{p}_1\rvert = \lvert\vec{p}_2\rvert = \sqrt{2}\frac{2\pi}{L}$

(Table continued)

TABLE II. *(Continued)*

$\frac{L}{2\pi}\vec{P}$	Little group LG	Irrep Λ	Angular momentum content	Operator number	Operator structure
(1,1,1)	C_{3v}	A_1	$J = 0, 1, \ldots$	1	K_i^{*+}
				2	K_{ti}^{*+}
				3	K_0^{+}
				4	$K\pi$ with $\lvert\vec{p}_1\rvert = 0$ and $\lvert\vec{p}_2\rvert = \sqrt{3}\frac{2\pi}{L}$
				5	$K\pi$ with $\lvert\vec{p}_1\rvert = \sqrt{3}\frac{2\pi}{L}$ and $\lvert\vec{p}_2\rvert = 0$
				6	$K\pi$ with $\lvert\vec{p}_1\rvert = \frac{2\pi}{L}$ and $\lvert\vec{p}_2\rvert = \sqrt{2}\frac{2\pi}{L}$
				7	$K\pi$ with $\lvert\vec{p}_1\rvert = \sqrt{2}\frac{2\pi}{L}$ and $\lvert\vec{p}_2\rvert = \frac{2\pi}{L}$
(1,1,1)	C_{3v}	E	$J = 1, 2, \ldots$	1	K_i^{*+}
				2	K_{ti}^{*+}
				3	$K\pi$ with $\lvert\vec{p}_1\rvert = \frac{2\pi}{L}$ and $\lvert\vec{p}_2\rvert = \sqrt{2}\frac{2\pi}{L}$
				4	$K\pi$ with $\lvert\vec{p}_1\rvert = \sqrt{2}\frac{2\pi}{L}$ and $\lvert\vec{p}_2\rvert = \frac{2\pi}{L}$

$$S_{seq_q}(t_{\rm snk},\vec{x}_{\rm snk};\Gamma(\vec{p});t_{\rm src},\vec{x}_{\rm src})^{ab}_{\alpha\beta} = \sum_{\vec{x},\beta',b'} D_q^{-1}(t_{\rm snk},\vec{x}_{\rm snk};t_{\rm src},\vec{x})^{a,b'}_{\alpha,\alpha'} \times \Gamma_{\alpha'\beta'} e^{i\vec{p}\cdot\vec{x}} S_l(t_{\rm src},\vec{x};t_{\rm src},\vec{x}_{\rm src})^{b'b}_{\beta',\beta}. \quad (41)$$

For the purpose of this calculation, we require only $\Gamma = \gamma_5$ to realize the pseudoscalar pion or kaon interpolators and $q = l/s$ for the second inversion of the light/strange Dirac operator.

In addition, we use time-slice-to-all stochastic propagators for the sink-to-sink quark propagation in Fig. 3(e). These follow from solving the Dirac equation with a fully time-diluted stochastic source

$$S_{st^{(2)}}(t_t,\vec{x}_{\rm snk};t_{\rm src},\vec{x}_{\rm src}) = \sum_{\vec{x},a',\alpha'} D_l^{-1}(t_{\rm snk},\vec{x}_{\rm snk};t_{\rm src},\vec{x})^{aa'}_{\alpha\alpha'} \times \eta^{(t_{\rm src})}(\vec{x})^{a'}_{\alpha'}\eta^{(t_{\rm src})}(\vec{x}_{\rm src})^{b*}_{\beta}. \quad (42)$$

The space-spin-color components of $\eta^{(t_{\rm src})}$ are independent, $\mathbb{Z}_2\times\mathbb{Z}_2$-distributed random numbers with zero mean and unit variance.

Finally, the all-source-to-all-sink quark propagation in Figs. 3(d) (lower fermion loop) and 3(f) are realized with stochastic source-time-slice-to-all propagators from spin-diluted noise sources based on the one-end trick [119],

$$S_{st^{(1)}}(t_{\rm snk},\vec{x}_{\rm snk};t_{\rm src},\vec{p}_{\rm src})^{a}_{\alpha\beta} = \sum_{x,a',\alpha'} D_l^{-1}(t_{\rm snk},\vec{x}_{\rm snk};x)^{aa'}_{\alpha\alpha'}\eta^{(t_{\rm src},\vec{p}_{\rm src},\beta)}(x)^{a'}_{\alpha'}, \quad (43)$$

where

$$\eta^{(t_{\rm src},\vec{p}_{\rm src},\beta)}(x)^{a'}_{\alpha'} = \delta_{\alpha',\beta}\delta_{t,t_{\rm src}}\eta(\vec{x})^{a'}e^{i\vec{p}_{\rm src}\cdot\vec{x}}, \quad (44)$$

with components $\eta(\vec{x})^{a'}$ again $\mathbb{Z}_2\times\mathbb{Z}_2$ noise.

V. SPECTRUM RESULTS

We extracted the energy levels $E_n^{\Lambda,\vec{P}}$ from the correlation matrices using the generalized eigenvalue problem [120,121]

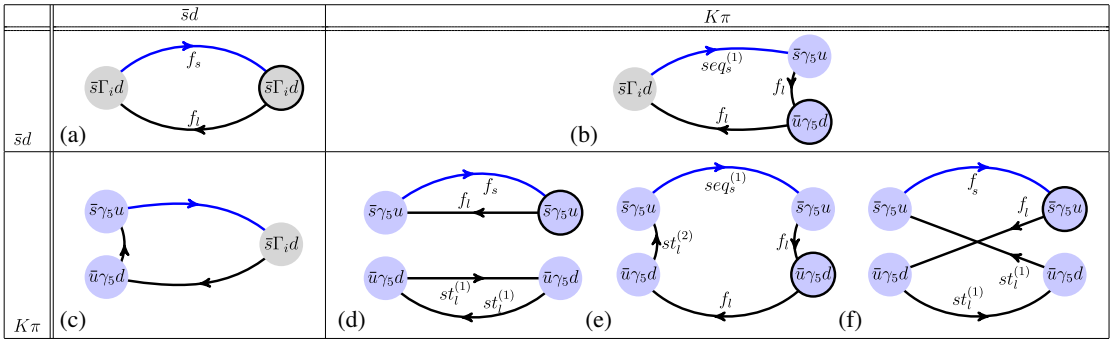

FIG. 3. The Wick contractions corresponding to the correlation matrix elements of type (a) $C_{\bar{q}q-\bar{q}q}$, (b,c) $C_{K\pi-\bar{q}q}$, (d) $C^{\rm direct}_{K\pi-K\pi}$, (e) $C^{\rm box}_{K\pi-K\pi}$, and (f) $C^{\rm cross}_{K\pi-K\pi}$. We do not directly compute diagram (c), since it can be obtained as the complex conjugate of diagram (b). The black circles outlining one of the interpolating fields in each diagram indicate the location of the point-to-all-propagator source.

$$\sum_B C^{\Lambda,\vec{P}}_{AB}(t)u^n_B(t) = \lambda^n(t,t_0)\sum_B C^{\Lambda,\vec{P}}_{AB}(t_0)u^n_B(t), \tag{45}$$

where n labels the eigenpair. Here, t_0 is a reference time slice whose variation does not affect noticeably the large-t behavior [118]. At large enough values of t and t_0, the eigenvalues $\lambda^n(t,t_0)$ take the form of a single exponential,

$$\lambda^n(t,t_0) = e^{-E^{\Lambda,\vec{P}}_n(t-t_0)}. \tag{46}$$

We can make some initial observations by looking at the effective energies

$$aE^n_{\text{eff}}(t) = \ln\frac{\lambda_n(t,t_0)}{\lambda_n(t+a,t_0)}, \tag{47}$$

shown in Fig. 4 for four different irreps of three different Little Groups. Dashed lines indicate the noninteracting energy levels of the $K\pi$ system with the pion and kaon momenta $|\vec{p}_1|$ and $|\vec{p}_2|$ used for the corresponding operator basis. In the plot for irrep T_{1u}, note that the highest three energy levels are shifted upward relative to the noninteracting energies. These states overlap most strongly (in relative terms) with the states created by the corresponding multihadron operators. The lowest energy level is an extra energy level whose occurrence is related to the presence of a narrow resonance (the K^*). This state overlaps most strongly with the states created by the quark-antiquark operators. Similarly, on the top-right plot ($\Lambda = A_{1g}$, $|\vec{P}|^2 = 0$), there is a downward shift with respect to the noninteracting energies from which we can expect an attractive interaction and a positive S-wave scattering phase shift. With the absence of an extra energy level, one cannot straightforwardly identify the presence of a resonance in the depicted energy range.

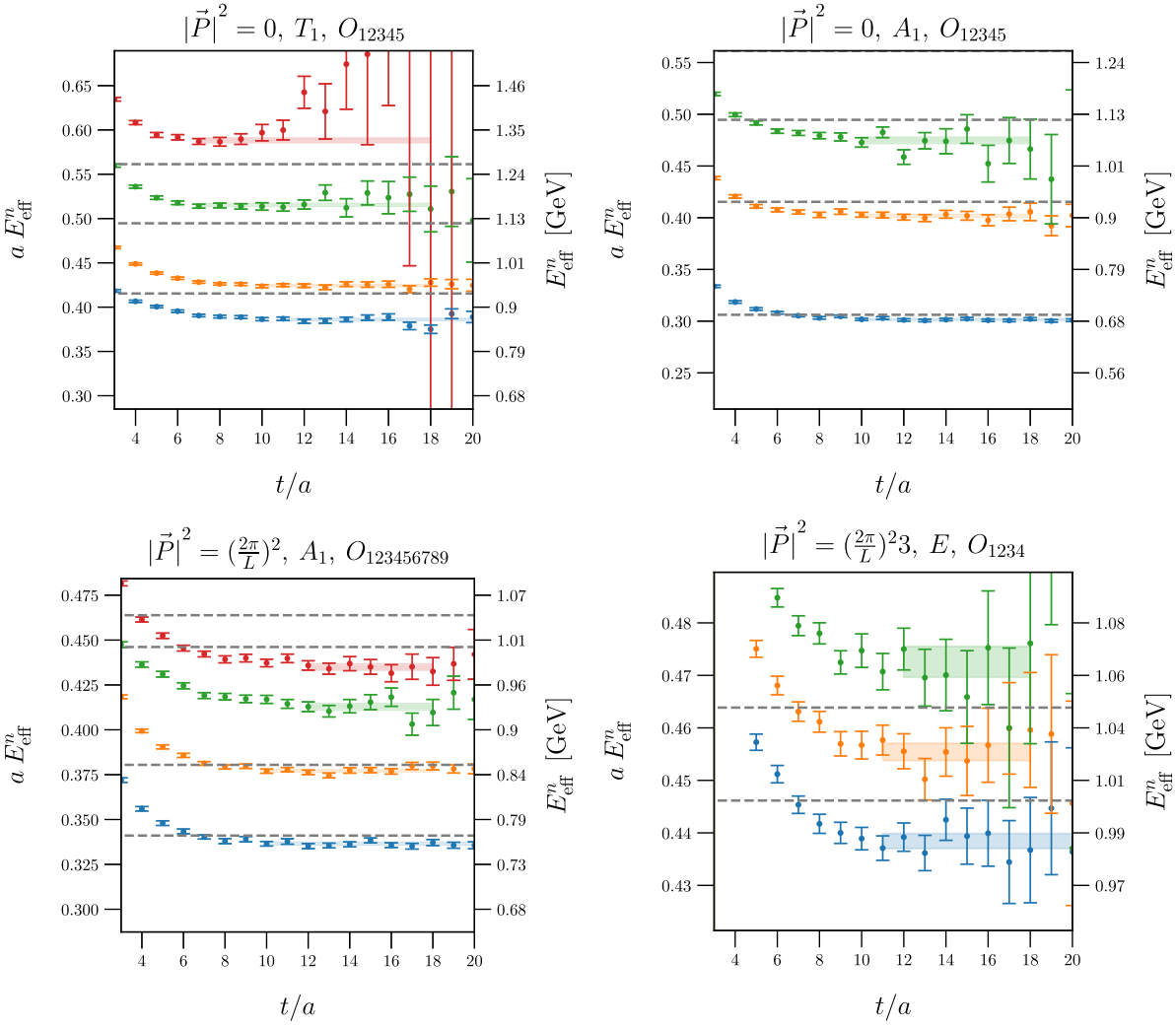

FIG. 4. Sample plots of effective energies [defined in Eq. (47)] from the D6 ensemble. The noninteracting energy levels are indicated with dashed lines. The results from single-exponential fits are shown as the shaded bands, indicating the $\pm 1\sigma$ energy range and the fit range.

Our main results for the energies $E_n^{\Lambda,\vec{P}}$ are obtained directly from single-exponential fits to the generalized eigenvalues $\lambda^n(t,t_0)$ and are given in Table III. Also shown in the table are the center-of-momentum-frame energies $\sqrt{s_n^{\vec{P},\Lambda}}$, which are related to the lattice-frame energy $E_n^{\Lambda,\vec{P}}$ through

$$\sqrt{s_n^{\vec{P},\Lambda}} = \sqrt{(E_n^{\vec{P},\Lambda})^2 - (\vec{P})^2}. \tag{48}$$

We have chosen the fit ranges such that the contributions from higher excited states are negligible compared to statistical uncertainty. We ensured this by varying the lower bound of the fit range, t_{min}, as shown in Figs. 5 and 6. In each case, the nominal value for t_{min}/a is chosen such that $\Delta E_{\mathrm{fwd}} = E|_{t_{\mathrm{min}}} - E|_{t_{\mathrm{min}}+a}$ is consistent with zero. Ancillary files with the central values of $a\sqrt{s_n^{\vec{P},\Lambda}}$ and their covariances for each ensemble are provided as part of Supplemental Material [122].

VI. LÜSCHER ANALYSIS

Assuming elasticity and neglecting exponential finite-volume effects, the energy levels of a two-particle system with total momentum $\vec{P}$ in a cubic box with periodic boundary conditions are given by the solutions of the Lüscher quantization condition

$$\det\left(\mathbb{1} + iT(\mathbb{1} + i\mathcal{M}^{\vec{P}})\right) = 0. \tag{49}$$

The object in parentheses is a matrix with indices $\ell m, \ell' m'$. The T-matrix introduced in Sec. II is diagonal,

$$T_{\ell m,\ell' m'} = T^{(\ell)}\delta_{\ell\ell'}\delta_{mm'}, \tag{50}$$

and for a single scattering channel as considered here, $T^{(\ell)}$ denotes the scattering amplitude for partial wave ℓ. The amplitudes $T^{(\ell)}$ depend only on the center-of-mass energy or, equivalently, the scattering momentum k. The elements of $\mathcal{M}^{\vec{P}}$ for $\ell, \ell' \leq 1$ are given by [62]

$$(\mathcal{M}^{\vec{P}}_{\ell m,\ell' m'}) = \begin{array}{c} \\ 00 \\ 10 \\ 11 \\ 1-1 \end{array} \begin{array}{c} \begin{array}{cccc} 00 & 10 & 11 & 1-1 \end{array} \\ \begin{pmatrix} w_{00} & i\sqrt{3}w_{10} & i\sqrt{3}w_{11} & i\sqrt{3}w_{1-1} \\ -i\sqrt{3}w_{10} & w_{00}+2w_{20} & \sqrt{3}w_{21} & \sqrt{3}w_{2-1} \\ i\sqrt{3}w_{1-1} & -\sqrt{3}w_{2-1} & w_{00}-w_{20} & -\sqrt{6}w_{2-2} \\ i\sqrt{3}w_{11} & -\sqrt{3}w_{21} & -\sqrt{6}w_{22} & w_{00}-w_{20} \end{pmatrix} \end{array}, \tag{51}$$

where the functions $w_{\ell m}$ depend on the scattering momentum k, the box size L, and the total momentum $\vec{P}$,

$$w_{\ell m} = w^{\vec{P}}_{\ell m}(k,L) = \frac{Z^{\vec{P}}_{\ell m}(1;(k\frac{L}{2\pi})^2)}{\gamma\pi^{3/2}\sqrt{2\ell+1}(k\frac{L}{2\pi})^{\ell+1}}. \tag{52}$$

Here, $Z^{\vec{P}}_{\ell m}(1;(k\frac{L}{2\pi})^2)$ is the generalized zeta function and $\gamma = E^{\vec{P}}/\sqrt{s}$ is the Lorentz boost factor. The matrix $\mathcal{M}^{\vec{P}}$ can be further simplified by taking into account the symmetries for a given Little Group $LG(\vec{P})$ and irreducible representation Λ [62]. Each irrep in principle contains infinitely many partial waves, the first few of which are listed in Table II (since the K and π are both spinless, we have $J = \ell$). However, the contributions from higher partial waves are increasingly suppressed, and we neglect the contributions from $\ell \geq 2$ in this work. This then leads to the following quantization conditions, where we write the scattering amplitudes $T^{(0)}$ and $T^{(1)}$ in terms of the phase shifts δ_0 and δ_1, respectively:

$$\vec{P} = \frac{2\pi}{L}(0,0,0), \qquad LG = O_h, \qquad \Lambda = A_{1g}:$$
$$\cot\delta_0 = w_{00}, \tag{53}$$

$$\vec{P} = \frac{2\pi}{L}(0,0,0), \quad LG = O_h, \quad \Lambda = T_{1u}: \ \cot\delta_1 = w_{00}, \tag{54}$$

$$\vec{P} = \frac{2\pi}{L}(0,0,1), \quad LG = C_{4v}, \quad \Lambda = A_1:$$
$$(\cot\delta_0 - w_{00})(\cot\delta_1 - w_{00} - 2w_{20}) - 3w_{10}^2 = 0, \tag{55}$$

$$\vec{P} = \frac{2\pi}{L}(0,0,1), \qquad LG = C_{4v}, \qquad \Lambda = E:$$
$$\cot\delta_1 = w_{00} - w_{20}, \tag{56}$$

$$\vec{P} = \frac{2\pi}{L}(0,1,1), \qquad LG = C_{2v}, \qquad \Lambda = A_1:$$
$$(\cot\delta_0 - w_{00})(\cot\delta_1 - w_{00} + w_{20} + i\sqrt{6}w_{22}) + 6iw_{11}^2 = 0, \tag{57}$$

$$\vec{P} = \frac{2\pi}{L}(0,1,1), \qquad LG = C_{2v}, \qquad \Lambda = B_1:$$
$$\cot\delta_1 = w_{00} + 2w_{20}, \tag{58}$$

$$\vec{P} = \frac{2\pi}{L}(0,1,1), \qquad LG = C_{2v}, \qquad \Lambda = B_2:$$
$$\cot\delta_1 = w_{00} - w_{20} - \sqrt{6}\,\mathrm{Im}[w_{22}], \tag{59}$$

TABLE III. Results of single-exponential fits to the generalized eigenvalues, for the two different ensembles, the different total momenta $\vec{P}$, and the different irreps Λ. We set $t_0/a = 3$ on the C13 ensemble and $t_0/a = 4$ on the D6 ensemble. Ancillary files with the central values of $a\sqrt{s_n^{\vec{P},\Lambda}}$ and their covariances for each ensemble are provided as part of Supplemental Material [122].

Ensemble	$\frac{L}{2\pi}\lvert\vec{P}\rvert$	Λ	n	Fit range	$\frac{\chi^2}{\mathrm{dof}}$	$aE_n^{\vec{P},\Lambda}$	$a\sqrt{s_n^{\vec{P},\Lambda}}$
C13	0	T_1	1	10–20	0.76	0.5189(17)	0.5189(17)
C13	0	A_1	1	9–20	1.14	0.48318(63)	0.48318(63)
C13	1	A_1	1	8–20	0.68	0.53809(74)	0.50099(79)
C13	1	A_1	2	8–20	0.29	0.5544(10)	0.5184(11)
C13	1	A_1	3	8–20	1.37	0.57660(89)	0.54214(94)
C13	1	E	1	8–20	0.97	0.5547(13)	0.5188(14)
C13	$\sqrt{2}$	A_1	1	9–20	0.48	0.5809(16)	0.5103(18)
C13	$\sqrt{2}$	A_1	2	8–18	0.83	0.5977(16)	0.5292(18)
C13	$\sqrt{2}$	A_1	3	8–18	0.44	0.6242(12)	0.5590(14)
C13	$\sqrt{2}$	B_2	1	8–20	1.12	0.5866(19)	0.5167(21)
C13	$\sqrt{2}$	B_2	2	9–20	0.84	0.6374(12)	0.5737(13)
C13	$\sqrt{2}$	B_1	1	9–20	0.90	0.5871(23)	0.5172(26)
C13	$\sqrt{3}$	A_1	1	7–20	0.81	0.6183(24)	0.5163(29)
C13	$\sqrt{3}$	A_1	2	7–18	1.18	0.6397(22)	0.5418(26)
C13	$\sqrt{3}$	A_1	3	7–18	0.42	0.6686(20)	0.5757(23)
C13	$\sqrt{3}$	E	1	8–20	0.94	0.6189(32)	0.5171(38)
C13	$\sqrt{3}$	E	2	8–18	1.01	0.6843(13)	0.5938(14)
D6	0	T_1	1	11–20	1.54	0.3861(11)	0.3861(11)
D6	0	T_1	2	10–18	0.38	0.4244(10)	0.4244(10)
D6	0	A_1	1	10–20	0.71	0.30162(71)	0.30162(71)
D6	0	A_1	2	10–18	0.22	0.4018(13)	0.4018(13)
D6	1	A_1	1	10–20	0.79	0.33657(73)	0.31007(80)
D6	1	A_1	2	10–18	0.96	0.37714(58)	0.35369(62)
D6	1	A_1	3	12–18	1.15	0.4128(18)	0.3915(19)
D6	1	A_1	4	12–18	0.19	0.4350(17)	0.4148(18)
D6	1	E	1	12–20	1.51	0.4072(15)	0.3856(16)
D6	1	E	2	9–18	0.63	0.45134(94)	0.43194(98)
D6	1	E	3	12–16	0.03	0.4694(17)	0.4508(18)
D6	$\sqrt{2}$	A_1	1	9–20	0.62	0.36787(82)	0.31789(95)
D6	$\sqrt{2}$	A_1	2	10–18	1.23	0.41041(82)	0.36629(92)
D6	$\sqrt{2}$	A_1	3	10–18	0.75	0.42372(97)	0.3811(11)
D6	$\sqrt{2}$	A_1	4	9–18	0.77	0.4412(13)	0.4005(15)
D6	$\sqrt{2}$	B_2	1	11–18	0.36	0.41064(76)	0.36655(85)
D6	$\sqrt{2}$	B_2	2	9–18	0.54	0.4414(15)	0.4007(16)
D6	$\sqrt{2}$	B_1	1	10–20	0.89	0.4294(14)	0.3874(16)
D6	$\sqrt{2}$	B_1	2	9–18	0.47	0.4775(13)	0.4402(14)
D6	$\sqrt{3}$	A_1	1	8–20	0.98	0.3966(12)	0.3254(15)
D6	$\sqrt{3}$	A_1	2	8–18	1.42	0.4397(13)	0.3767(15)
D6	$\sqrt{3}$	A_1	3	8–18	1.26	0.4497(15)	0.3884(18)
D6	$\sqrt{3}$	A_1	4	9–18	0.82	0.4659(20)	0.4070(23)
D6	$\sqrt{3}$	E	1	11–20	0.30	0.4385(14)	0.3753(17)
D6	$\sqrt{3}$	E	2	11–18	0.38	0.4554(17)	0.3950(19)
D6	$\sqrt{3}$	E	3	12–18	0.39	0.4726(29)	0.4146(34)

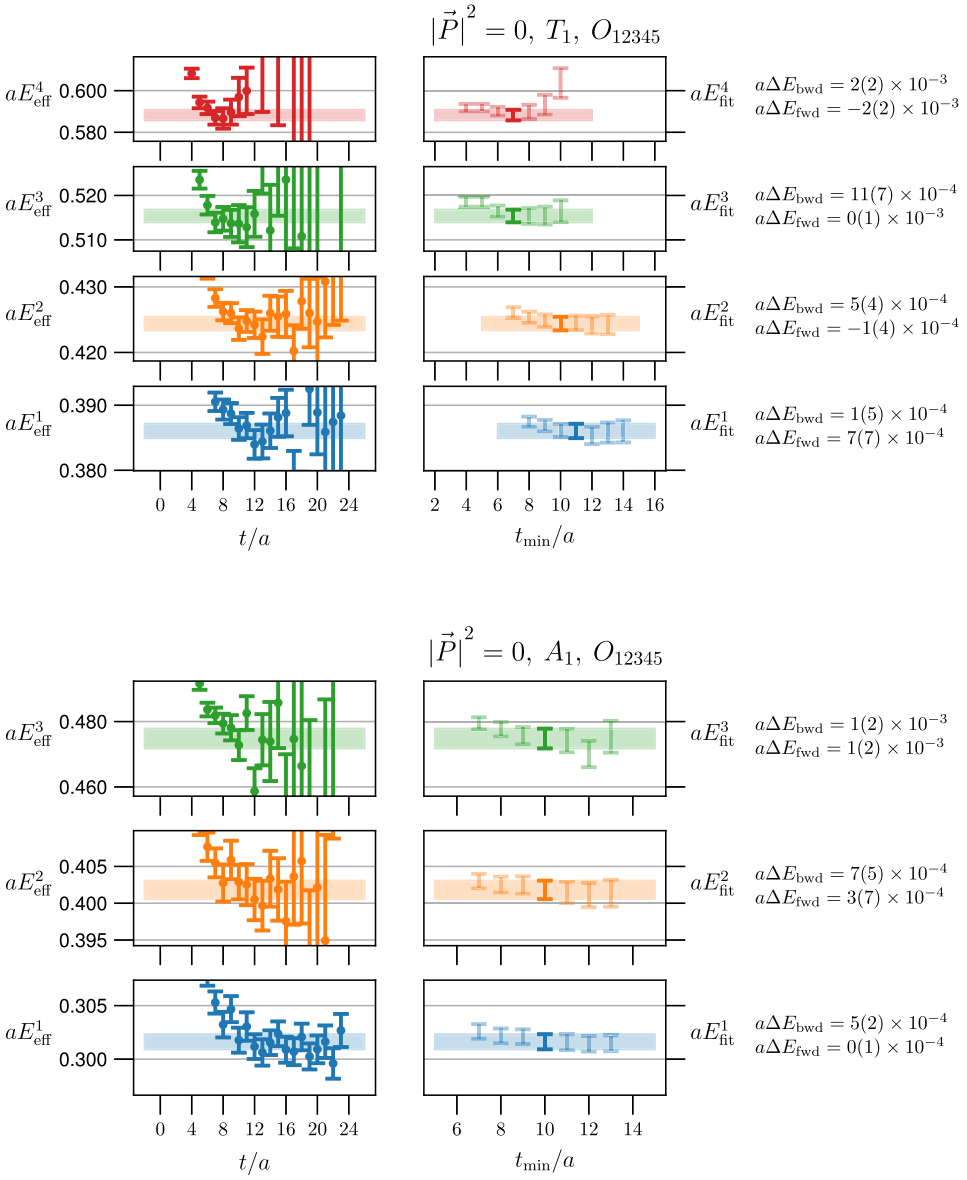

FIG. 5. Sample plots illustrating our tests of the stability of the fitted energies under variations of the lower bound of the fit range, $t_{\rm min}$. The left panels show the effective-energy plots for the generalized eigenvalues. The center panels show the fitted energies as a function of $t_{\rm min}$. On the right, we give the changes in the fitted energies when shifting $t_{\rm min}$ by one lattice step: $\Delta E_{\rm bwd} = E|_{t_{\rm min}-a} - E|_{t_{\rm min}}$ and $\Delta E_{\rm fwd} = E|_{t_{\rm min}} - E|_{t_{\rm min}+a}$, for our nominal choice of $t_{\rm min}$. The results shown here are from the D6 ensemble for the irreps A_{1g} and T_{1u} of the Little Group O_h.

$$\vec{P} = \frac{2\pi}{L}(1,1,1), \qquad LG = C_{3v}, \qquad \Lambda = A_1: \\ (\cot\delta_0 - w_{00})(-\cot\delta_1 + w_{00} - 2i\sqrt{6}w_{22}) \\ + 9w_{10}^2 = 0, \tag{60}$$

$$\vec{P} = \frac{2\pi}{L}(1,1,1), \qquad LG = C_{3v}, \qquad \Lambda = E: \\ \cot\delta_1 = w_{00} + i\sqrt{6}w_{22}. \tag{61}$$

Note that at nonzero momenta the quantization conditions in the A_1 irreps depend on both the S-wave and the P-wave phase shifts. This mixing between even and odd partial waves occurs because the reciprocal space of momenta in the unequal-mass $K\pi$ system lacks inversion symmetry [62]. Traditionally, the Lüscher method has often been used to map individual energy levels on the lattice to individual phase shift values at the corresponding center-of-mass energies. However, this is no longer possible in the A_1 irreps with partial-wave mixing. Equation (55), for example, has the two unknowns $\delta_0(k_n^{\vec{P},A_1})$ and $\delta_1(k_n^{\vec{P},A_1})$, and it

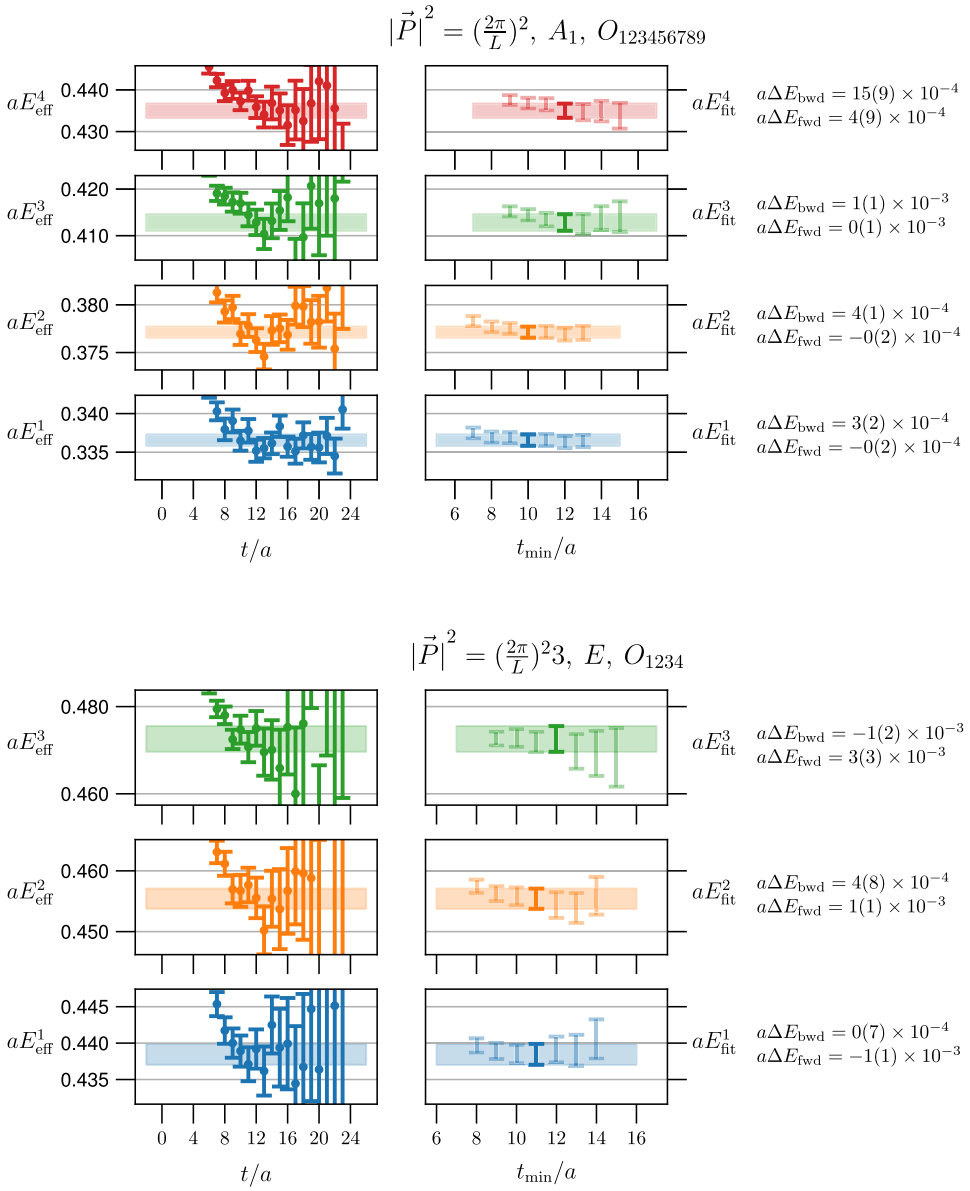

FIG. 6. Like Fig. 5, but for irreps A_1 and E of the Little Groups C_{4v} and C_{3v}, respectively.

does not help to combine Eqs. (55) and (56) either, because the solutions of Eq. (56) occur at different values of the scattering momentum, $k_n^{\vec{P},E}$. Since we want to use all irreps, we follow a different approach [123], in which we parametrize the energy dependence of the phase shifts δ_0 and δ_1 using the models discussed in Sec. II, and then perform a global fit of the model parameters for both the S- and P-waves to all energy levels by minimizing the following χ^2 function:

$$\chi^2 = \sum_{\vec{P},\Lambda,n} \sum_{\vec{P}',\Lambda',n'} [C^{-1}]_{\vec{P},\Lambda,n;\vec{P}',\Lambda',n'} \left(\sqrt{s_n^{\Lambda,\vec{P}}}^{\rm [data]} - \sqrt{s_n^{\Lambda,\vec{P}}}^{\rm [model]} \right) \times \left(\sqrt{s_{n'}^{\Lambda',\vec{P}'}}^{\rm [data]} - \sqrt{s_{n'}^{\Lambda',\vec{P}'}}^{\rm [model]} \right). \quad (62)$$

Here, $[C^{-1}]$ is the data covariance matrix of the spectrum determined on the lattice, and $\sqrt{s_n^{\Lambda,\vec{P}}}^{\rm [model]}$ is obtained from the parametrized scattering amplitudes using the Lüscher quantization conditions.[2] We fit 17 energy levels on the `C13` ensemble and 26 levels on the `D6` ensemble, as listed in Table III. In choosing these energy levels, we have stayed further below the $K\eta$ threshold, approximately $0.95\sqrt{s_{K\eta}}$, determined through Eq. (27) in order to safely avoid effects from the $K\eta$ threshold, the $K^\star(1410)$ resonance, or rescattering from three particle channels [22]. In practice,

[2]In Ref. [118], we demonstrated that the results of this approach are consistent with those from the traditional two-step approach (when applicable) of first extracting individual phase shifts followed by a fit of a model to the phase shifts.

we found it helpful to obtain initial guesses for the P-wave model parameters using an initial fit to only those irreps without S-wave contributions, followed by the full fit to all irreps. The results for the P-wave parameters from the full fits are consistent with the results from the reduced fits but are about 10% more precise. Moreover, we performed a combined fit with a reduced set of irreps (T_{1u}, A_{1g}, and C_{4v}'s A_1), which, apart from increasing the uncertainty in some parameters compared to using the full list, has also proven to worsen the χ^2/dof minimum to an unacceptable value. This further justifies the use of data from higher momentum frames. On each ensemble, we performed four different full fits that differ in the type of parametrization used for the S-wave amplitude: Chung's parametrization [Eq. (13)], effective-range expansion [Eq. (19)], Bugg's parametrization [Eq. (22)], and conformal-map parametrization [Eq. (24)]. The parametrization for the P-wave amplitude was always of the form given in Eq. (13). The best-fit parameters and χ^2 values of the full fits are given in Tables V and VI in the Appendix.

VII. RESULTS FOR THE PHASE SHIFTS AND POLE POSITIONS

The phase-shift curves obtained from the four different fits and the two ensembles are presented in Fig. 7. In addition, we determined the positions of the closest T-matrix poles in the complex $\sqrt{s}$ plane, which are associated with the κ and K^* resonances. The pole positions are shown in Fig. 8 and are listed in Table IV. All poles are located on the second Riemann sheet. In the following, we discuss our observations separately for the S- and P-waves.

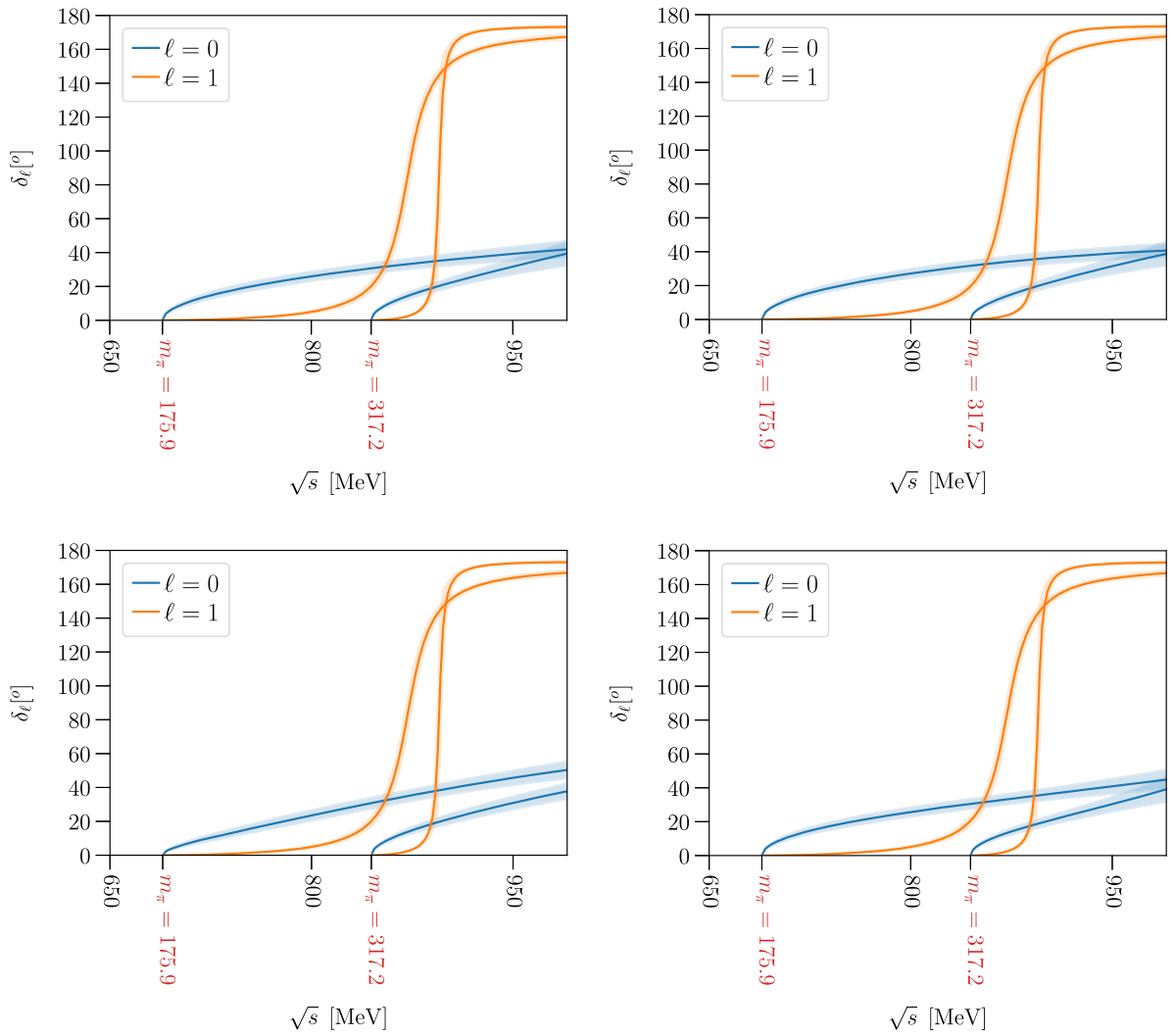

FIG. 7. S- and P-wave phase shift results from both ensembles, labeled here by to their pion masses. The four different plots differ in the type of parametrization used for the S-wave amplitude. From top-left to right-bottom: Chung's parametrization [Eq. (13)], effective-range expansion [Eq. (19)], Bugg's parametrization [Eq. (22)], and conformal-map parametrization [Eq. (24)]. The parametrization for the P-wave amplitude was always of the form given in Eq. (13).

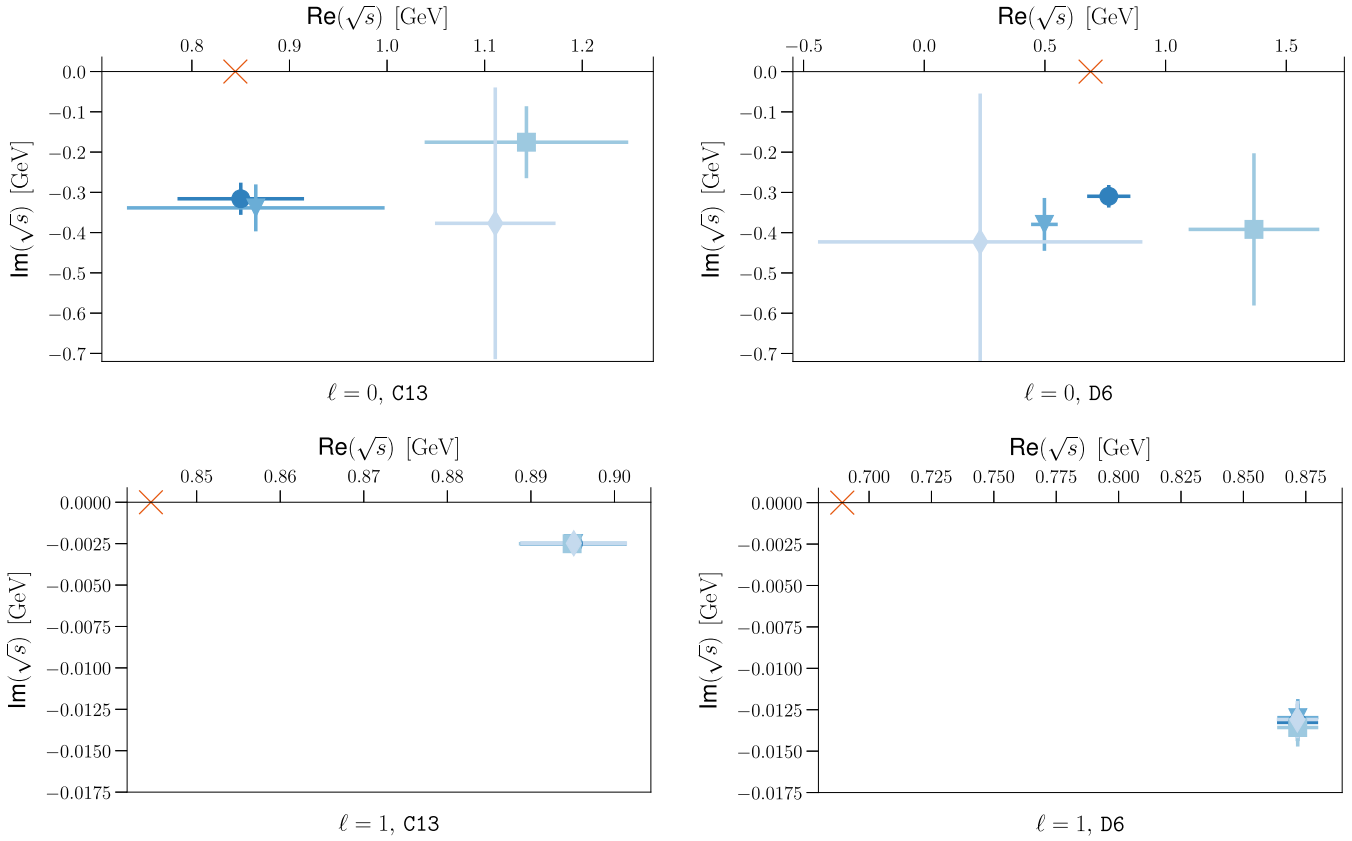

FIG. 8. T-matrix pole positions for the S-wave (top) and P-wave (bottom). The plots on the left show the results from the C13 ensemble [$m_\pi = 317.2(2.2)$ MeV], while the plots on the right show the results from the D6 [$m_\pi = 175.9(1.8)$ MeV] ensemble. In each plot, the four different data points correspond to four different parametrizations of the S-wave amplitude. We can see a better stability of the S-wave pole position for the parametrizations with an Adler zero.

A. S-wave scattering

The S-wave phase-shift curves from the four different parametrizations are in reasonable agreement with each other, given the uncertainties. We observe that the phase shifts remain below 80° in the energy region considered. Even though there is little model dependence in the phase-shift curves for real-valued $\sqrt{s}$, the positions of the resulting poles of the scattering amplitude vary widely between the different parametrizations. Moreover, some of the parametrizations lead to a much stronger dependence on the pion mass than others:

(i) The ERE parametrization [Eq. (19)] yields a pole at $[1.11(6) - 0.38(34)i]$ GeV on the C13 ensemble and at $[0.33(23) - 0.35(22)i]$ GeV on the D6 ensemble. This change is significantly larger than expected from the relatively minor change in the quark masses. Note that the ERE is meant to describe the behavior near the threshold and likely becomes unreliable in the upper range of our energy region.

(ii) The poles for Chung's K-matrix parametrization without an Adler zero [Eq. (13)] appear above

TABLE IV. Pole positions the S-wave and P-wave scattering amplitudes on the C13 [$m_\pi = 317.2(2.2)$ MeV] and D6 [$m_\pi = 175.9(1.8)$ MeV] ensembles.

S-wave parametrization	Ensemble	S-wave T-matrix poles (GeV)	P-wave T-matrix poles (GeV)
Conformal map	C13	$0.86(12) - 0.309(50)i$	$0.8951(64) - 0.00250(21)i$
	D6	$0.499(55) - 0.379(66)i$	$0.8718(82) - 0.0130(11)i$
Bugg's parametrization	C13	$0.850(65) - 0.315(40)i$	$0.8951(64) - 0.00250(21)i$
	D6	$0.765(90) - 0.310(28)i$	$0.8717(82) - 0.0133(11)i$
Effective-range expansion	C13	$1.111(62) - 0.38(34)i$	$0.8951(64) - 0.00248(21)i$
	D6	$0.23(67) - 0.42(37)i$	$0.8716(82) - 0.0131(11)i$
Chung's parametrization	C13	$1.14(10) - 0.176(89)i$	$0.8949(64) - 0.00250(21)i$
	D6	$1.37(27) - 0.39(19)i$	$0.8718(82) - 0.0136(11)i$

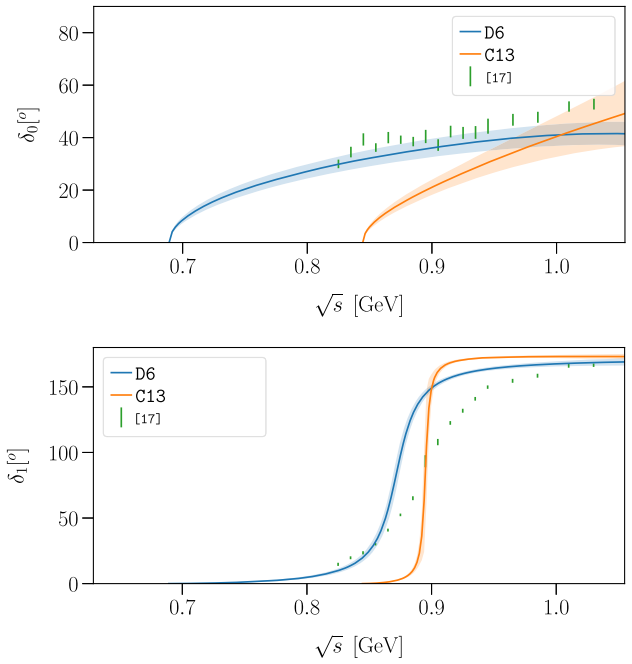

FIG. 9. Phase shift results, using the conformal-map parametrization for the S-wave and Chung's parametrization for the P-wave, compared to experimental results from Ref. [17]. The fitted parameters with the corresponding covariances used to produce these plots are included in Supplemental Material [122].

1.1 GeV—in the region where we do not have data points to fully constrain the amplitude—with only mild dependence on the quark masses. What may be happening is that this fit is sensing the $K_0^*(1430)$ resonance located not that far away [22].

(iii) For the conformal-map-based parametrization [Eq. (24)] and Bugg's parametrization [Eq. (22)], which both include an Adler zero, the poles appear near $[0.7 - 0.3i]$ GeV consistently for the two pion masses and consistently for the two parametrizations. On the lower-pion-mass ensemble in particular, these parametrizations also yield much smaller statistical uncertainties for the pole locations.

In summary, the poles of the S-wave amplitude are significantly more stable for parametrizations incorporating an Adler zero. Because the conformal-map parametrization describes the data on the lower-pion-mass ensemble (D6) better than Bugg's parametrization, we choose the conformal-map parametrization as our nominal parametrization.

In Fig 9, we compare the phase-shift curves from this parametrization to experimental results from Ref. [17]. We see that the S-wave phase-shift curves approach the experimental data as the pion mass is lowered toward its physical value. The pion mass of the D6 ensemble is nearly physical, and the resulting curve is very close to the data. The behavior of the curve as a function of the pion mass seen here is also consistent with the lattice results in Ref. [92] at a higher pion mass.

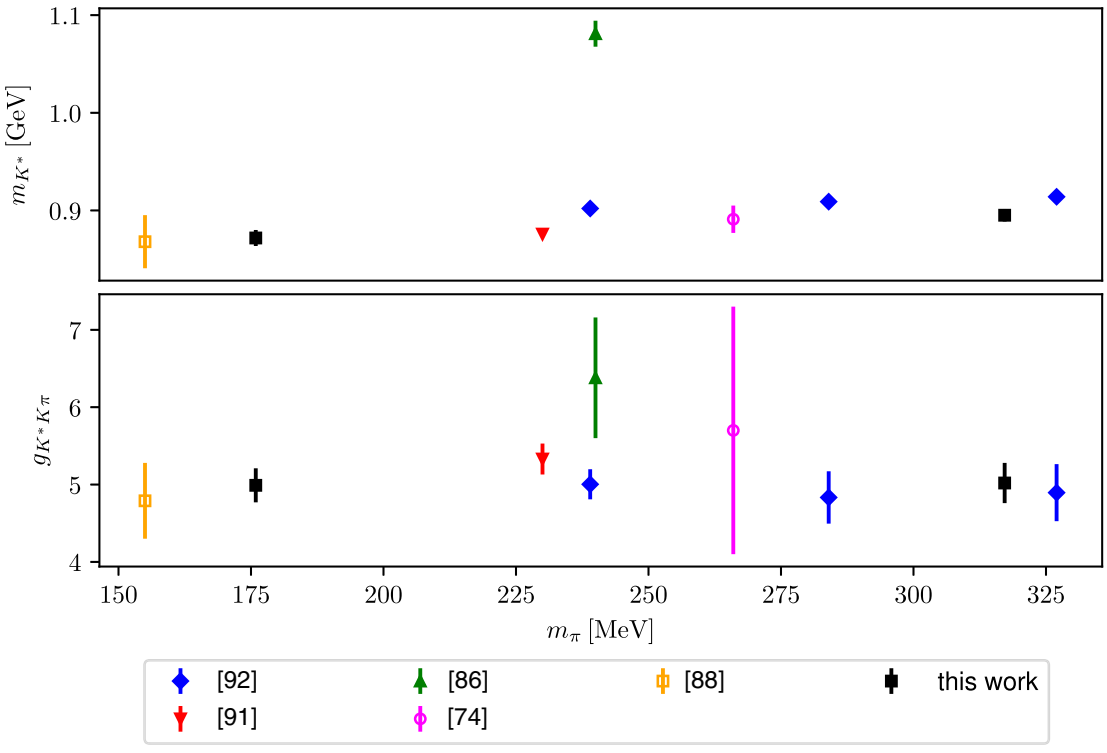

FIG. 10. Comparison between different lattice-QCD results for the K^* mass and its coupling to the $K\pi$ channel, plotted as a function of the pion mass. The references are Wilson *et al.* [92], Fu and Fu [86], Bali *et al.* [88], Brett *et al.* [91], and Lang *et al.* [74]. Open symbols indicate $N_f = 2$ results, and the filled symbols indicate $N_f = 2 + 1$ results.

B. P-wave scattering

The results presented in Figs. 7 and 8 and Table IV were all obtained with Chung's K-matrix parametrization, Eq. (13), for the P-wave. While we explored other P-wave parametrizations that do not include Blatt-Weisskopf barrier factors, we found little variation (an explicit comparison can be found for $I = 1$ $\pi\pi$ scattering in Ref. [118], which also showed no significant variation). Furthermore, the P-wave phase-shift curves and pole locations do not significantly depend on the choice of the S-wave parametrization, which confirms that partial-wave mixing between $\ell = 0$ and $\ell = 1$ is under good control. We choose the same combination of parametrizations as above (Chung's parametrization for the P-wave combined with the conformal map for the S wave) for our nominal results for the P wave.

A comparison of the phase-shift curves for the two different pion masses with experimental data [17] is shown in Fig. 9. A clear resonance shape is observed for both pion masses. In this channel, the resonance width $\Gamma_{K^*\to K\pi} = -2\mathrm{Im}(\sqrt{s}_R)$, where $\sqrt{s}_R$ is the location of the pole, depends strongly on the pion mass due to the large change in available phase space. We find

$$\Gamma^{\mathtt{C13}}_{K^*\to K\pi} = (4.99 \pm 0.41)\ \mathrm{MeV}, \tag{63}$$

$$\Gamma^{\mathtt{D6}}_{K^*\to K\pi} = (26.0 \pm 2.2)\ \mathrm{MeV}, \tag{64}$$

while the value in nature is 50.8(0.9) MeV [22]. Consequently, even at the close-to-physical pion mass of the D6 ensemble, the phase shift curve is still noticeably steeper than in nature. In this situation, it is more appropriate to consider the $K^*K\pi$ coupling $g_{K^*K\pi}$, which can be obtained from the decay width through

$$\Gamma_{K^*\to K\pi} = \frac{g^2_{K^*K\pi}}{6\pi}\frac{k^3_*}{\mathrm{Re}(\sqrt{s}_R)^2}, \tag{65}$$

where k_* is the scattering momentum for $\sqrt{s} = \mathrm{Re}(\sqrt{s}_R)$. This gives

$$g^{\mathtt{C13}}_{K^*K\pi} = 5.02(26), \tag{66}$$

$$g^{\mathtt{D6}}_{K^*K\pi} = 4.99(22). \tag{67}$$

These values are consistent with each other and also consistent with similar calculations [88,92]. Our results are slightly below the experimental value of $g_{K^*K\pi} = 5.603(4)$. A comparison of our results for m_{K^*} and $g_{K^*K\pi}$ with previous lattice results is shown in Fig. 10.

VIII. CONCLUSIONS

We have obtained precise results for the $I = 1/2$ S- and P-wave $K\pi$ scattering phase shifts as functions of the center-of-mass energy up to 1.1 GeV, for quark masses corresponding to $m_\pi \approx 176$ MeV and $m_\pi \approx 317$ MeV. We also determined the positions of the closest poles in the scattering amplitudes, which we identify with the $K^*_0(700)$ (also referred to as κ) and $K^*(892)$ resonances.

For the S-wave amplitude, we investigated several different parametrizations proposed in the literature, some including an Adler zero and some without it. All parametrizations considered, including the effective-range expansion that is similar to the widely used LASS parametrization [17], describe the phase shifts well for real $\sqrt{s}$ in the energy region considered. However, we found that the pole positions are stable only for those parametrizations that include an Adler zero. Using a conformal-map-based parametrization with an Adler zero, we found the poles in the S-wave scattering amplitude at $[0.86(12) - 0.309(50)i]$ GeV for $m_\pi \approx 317$ MeV and $[0.499(55) - 0.379(66)i]$ GeV for $m_\pi \approx 176$ MeV. Despite the unphysical pion masses and the lack of continuum extrapolations, these results are consistent with the κ pole position extracted from experiments as reported by the Particle Data Group [22].

Earlier lattice calculations at a heavier pion mass of $m_\pi \approx 390$ MeV performed by the Hadron Spectrum Collaboration [89,90] found the κ as a bound state. More recently, the same collaboration reported results for a wider range of pion masses down to approximately 200 MeV [92]. Investigating a large number of parametrizations, the authors did not find a sufficiently unique result to report numerically. For the parametrizations inspired by unitarized chiral perturbation theory, they did, however, find a κ pole with a real part near the $K\pi$ threshold and a large imaginary part. This is consistent with our findings for parametrizations that include the Adler zero.

In the vector channel, our results for the K^* mass and width have high statistical precision. Since the K^* width depends strongly on the pion mass through kinematic effects, it is more appropriate to consider the $K^*K\pi$ coupling. Our results for this coupling and for the K^* mass are compared with previous lattice results [74,86,88,89,91,92] in Fig. 10. Note that the calculations were performed with different numbers of flavors, different gluon and fermion discretizations, and different procedures to set the lattice scale; none of the calculations included a continuum extrapolation. Keeping in mind these caveats, we note that our results for both $g_{K^*K\pi}$ and m_{K^*} agree well with previous calculations, except for the higher mass obtained by Fu and Fu using a staggered fermion action [86]. Apart from this outlier, the results for m_{K^*} show only very mild quark-mass dependence, while $g_{K^*K\pi}$ has no discernible quark-mass dependence, similar to $g_{\rho\pi\pi}$ [118]. Furthermore, the results from $N_f = 2 + 1$ and $N_f = 2$ ensembles appear to follow common straight lines.

The calculations performed here can also be used in future lattice determinations of $1 \to 2$ transition matrix elements of external currents with the same $K\pi$ states. The scattering amplitudes are needed to map the finite-volume matrix elements to infinite-volume matrix elements via the

formalism of Ref. [93], as has already been done for $\pi\gamma^* \to \pi\pi$ [124,125]. Such a calculation will be particularly important for rare $B \to K\pi\ell^+\ell^-$ decays [8–15,126].

ACKNOWLEDGMENTS

We thank Kostas Orginos, Balint Joó, Robert Edwards, and their collaborators for providing the gauge-field configurations. Computations for this work were carried out in part on 1) facilities of the USQCD Collaboration, which are funded by the Office of Science of the U.S. Department of Energy; 2) facilities of the Leibniz Supercomputing Centre, which is funded by the Gauss Centre for Supercomputing; 3) facilities at the National Energy Research Scientific Computing Center, a DOE Office of Science User Facility supported by the Office of Science of the U.S. Department of Energy under Contract No. DE-AC02-05CH1123; 4) facilities of the Extreme Science and Engineering Discovery Environment [127], which is supported by National Science Foundation Grant No. ACI-1548562; and 5) the Oak Ridge Leadership Computing Facility, which is a DOE Office of Science User Facility supported under Contract DE-AC05-00OR22725. S. M. is supported by the U.S. Department of Energy, Office of Science, Office of High Energy Physics under Award No. DE-SC0009913. M. P. gratefully acknowledges support by the Sino-German collaborative research center CRC-110. J. N. and A. P. are supported in part by the U.S. Department of Energy, Office of Nuclear Physics under Grants No. DE-SC0011090 and No. DE-SC0018121, respectively. G. R. is supported by the U.S. Department of Energy, Office of Science, Office of Nuclear Physics, under Contract No. DE-SC0012704 (BNL). L. L. acknowledges support from the U.S. Department of Energy, Office of Science, through Contracts No. DE-SC0019229 and No. DE-AC05-06OR23177 (JLAB). S. S. is supported by the National Science Foundation under CAREER Grant No. PHY-1847893 and by the RHIC Physics Fellow Program of the RIKEN BNL Research Center. Notice: This manuscript has been authored by employees of Brookhaven Science Associates, LLC, under Contract No. DE-SC0012704 with the U.S. Department of Energy. The publisher by accepting the manuscript for publication acknowledges that the United States Government retains a non-exclusive, paid-up,irrevocable, world-wide license to publish or reproduce the published form of this manuscript, or allow others to do so, for United States Government purposes. The views and opinions of authors expressed herein do not necessarily state or reflect those of the United States Government or any agency thereof.

APPENDIX: FIT PARAMETERS OF SCATTERING AMPLITUDES

The fit parameters for the scattering amplitudes are presented in Tables V and VI.

TABLE V. Fit results for the K-matrix parameters from the `C13` ensemble with $m_\pi \approx 317$ MeV. The type of parametrization for the P-wave is always the same (Chung's parametrization), while the parametrization for the S-wave changes and is given in the leftmost column. Here, a denotes the lattice spacing.

S-wave parametrization	Fit parameters	χ^2/dof
Conformal map	$g_1^0 a = 0.0682 \pm 0.0025$ $(m_1 a)^2 = 0.2676 \pm 0.0012$ $R_1 a^{-1} = 0 \pm 170$ $B_0 a^2 = 0.174 \pm 0.030$ $B_1 a^2 = -0.05 \pm 0.15$	0.764
Bugg's parametrization	$g_1^0 a = 0.0683 \pm 0.0025$ $(m_1 a)^2 = 0.2677 \pm 0.0012$ $R_1 a^{-1} = 0 \pm 17$ $G_0^0 a = 4.5 \pm 8.6$ $(m_0 a)^2 = 2.1 \pm 3.6$	0.761
Effective-range expansion	$g_1^0 a = 0.0680 \pm 0.0025$ $(m_1 a)^2 = 0.2677 \pm 0.0012$ $R_1 a^{-1} = 1 \pm 7.0$ $c_0 a = 0.248 \pm 0.039$ $c_1 a^2 = -3.3 \pm 2.5$	0.773
Chung's parametrization	$g_1^0 a = 0.0684 \pm 0.0025$ $(m_1 a)^2 = 0.2676 \pm 0.0012$ $R_1 a^{-1} = 0 \pm 20$ $g_0^0 a = 0.44 \pm 0.10$ $(m_0 a)^2 = 0.448 \pm 0.081$	0.753

TABLE VI. Like Table V, but for the `D6` ensemble with $m_\pi \approx 176$ MeV.

S-wave parametrization	Fit parameters	χ^2/dof
Conformal map	$g_1^0 a = 0.0894 \pm 0.0037$ $(m_1 a)^2 = 0.15046 \pm 0.00086$ $R_1 a^{-1} = 0 \pm 23$ $B_0 a^2 = 0.086 \pm 0.011$ $B_1 a^2 = 0.106 \pm 0.025$	0.958
Bugg's parametrization	$g_1^0 a = 0.0904 \pm 0.0037$ $(m_1 a)^2 = 0.15045 \pm 0.00086$ $R_1 a^{-1} = 0 \pm 280$ $G_0^0 a = 20 \pm 310$ $(m_0 a)^2 = 5 \pm 88$	1.44
Effective-range expansion	$g_1^0 a = 0.0898 \pm 0.0037$ $(m_1 a)^2 = 0.15040 \pm 0.00086$ $R_1 a^{-1} = 1.1 \pm 9.7$ $c_0 a = 0.173 \pm 0.030$ $c_1 a^2 = -0.7 \pm 2.0$	0.926
Chung's parametrization	$g_1^0 a = 0.0915 \pm 0.0037$ $(m_1 a)^2 = 0.15048 \pm 0.00086$ $R_1 a^{-1} = 1.5 \pm 7.0$ $g_0^0 a = 0.49 \pm 0.15$ $(m_0 a)^2 = 0.36 \pm 0.12$	0.875

[1] C. B. Lang, The πK scattering and related processes, Fortschr. Phys. **26**, 509 (1978).

[2] A. Bevan *et al.* (*BABAR* and Belle Collaborations), The physics of the B factories, Eur. Phys. J. C **74**, 3026 (2014).

[3] W. Altmannshofer *et al.* (Belle-II Collaboration), The Belle II physics book, Prog. Theor. Exp. Phys. **2019**, 123C01 (2019).

[4] R. Aaij *et al.* (LHCb Collaboration), Physics case for an LHCb upgrade II—Opportunities in flavour physics, and beyond, in the HL-LHC era, arXiv:1808.08865.

[5] D. Asner *et al.*, Physics at BES-III, Int. J. Mod. Phys. A **24**, 499 (2009).

[6] M. Ablikim *et al.*, Future physics programme of BESIII, Chin. Phys. C **44**, 040001 (2020).

[7] R. Aaij *et al.* (LHCb Collaboration), Measurements of CP violation in the three-body phase space of charmless $B^{\pm}$ decays, Phys. Rev. D **90**, 112004 (2014).

[8] R. Aaij *et al.* (LHCb Collaboration), Differential branching fraction and angular analysis of the decay $B^0 \to K^{*0}\mu^+\mu^-$, J. High Energy Phys. 08 (2013) 131.

[9] R. Aaij *et al.* (LHCb Collaboration), Measurement of Form-Factor-Independent Observables in the Decay $B^0 \to K^{*0}\mu^+\mu^-$, Phys. Rev. Lett. **111**, 191801 (2013).

[10] S. Descotes-Genon, J. Matias, and J. Virto, Understanding the $B \to K^*\mu^+\mu^-$ anomaly, Phys. Rev. D **88**, 074002 (2013).

[11] R. R. Horgan, Z. Liu, S. Meinel, and M. Wingate, Calculation of $B^0 \to K^{*0}\mu^+\mu^-$ and $B_s^0 \to \phi\mu^+\mu^-$ Observables Using Form Factors from Lattice QCD, Phys. Rev. Lett. **112**, 212003 (2014).

[12] R. Aaij *et al.* (LHCb Collaboration), Test of lepton universality with $B^0 \to K^{*0}\ell^+\ell^-$ decays, J. High Energy Phys. 08 (2017) 055.

[13] J. Aebischer, W. Altmannshofer, D. Guadagnoli, M. Reboud, P. Stangl, and D. M. Straub, B-decay discrepancies after Moriond 2019, Eur. Phys. J. C **80**, 252 (2020).

[14] M. Algueró, B. Capdevila, A. Crivellin, S. Descotes-Genon, P. Masjuan, J. Matias, M. Novoa, and J. Virto, Emerging patterns of new physics with and without lepton flavour universal contributions, Eur. Phys. J. C **79**, 714 (2019); Eur. Phys. J. C **80**, 511(A) (2020).

[15] R. Aaij *et al.* (LHCb Collaboration), Measurement of CP-Averaged Observables in the $B^0 \to K^{*0}\mu^+\mu^-$ Decay, Phys. Rev. Lett. **125**, 011802 (2020).

[16] P. Estabrooks, R. K. Carnegie, A. D. Martin, W. M. Dunwoodie, T. A. Lasinski, and D. W. G. S. Leith, Study of $K\pi$ scattering using the reactions $K^{+-}p \to K^{+-}\pi^+n$ and $K^{+-}p \to K^{+-}\pi^-\Delta^{++}$ at 13 GeV/c, Nucl. Phys. **B133**, 490 (1978).

[17] D. Aston *et al.*, A study of $K^-\pi^+$ scattering in the reaction $K^-p \to K^-\pi^+n$ at 11 GeV/c, Nucl. Phys. **B296**, 493 (1988).

[18] B. Adeva *et al.* (DIRAC Collaboration), First πK atom lifetime and πK scattering length measurements, Phys. Lett. B **735**, 288 (2014).

[19] O. E. Gorchakov and L. L. Nemenov, The estimation of production rates of π^+K^-, π^-K^+ and $\pi^+\pi^-$ atoms in proton–nucleus interactions at 450 GeVc^{-1}, J. Phys. G **43**, 095004 (2016).

[20] S. Adhikari *et al.* (GlueX Collaboration), Strange hadron spectroscopy with a secondary K_L beam at glueX, arXiv:1707.05284.

[21] S. N. Cherry and M. R. Pennington, There is no $\kappa(900)$, Nucl. Phys. **A688**, 823 (2001).

[22] M. Tanabashi *et al.* (Particle Data Group Collaboration), Review of particle physics, Phys. Rev. D **98**, 030001 (2018).

[23] J. Gasser and H. Leutwyler, Chiral perturbation theory: Expansions in the mass of the strange quark, Nucl. Phys. **B250**, 465 (1985).

[24] V. Bernard, N. Kaiser, and U. G. Meissner, πK scattering in chiral perturbation theory to one loop, Nucl. Phys. **B357**, 129 (1991).

[25] S. Ishida, M. Ishida, T. Ishida, K. Takamatsu, and T. Tsuru, Analysis of $K\pi$ scattering phase shift and existence of $\kappa(900)$ particle, Prog. Theor. Phys. **98**, 621 (1997).

[26] J. A. Oller, E. Oset, and J. R. Pelaez, Nonperturbative Approach to Effective Chiral Lagrangians and Meson Interactions, Phys. Rev. Lett. **80**, 3452 (1998).

[27] J. A. Oller, E. Oset, and J. R. Pelaez, Meson meson interaction in a nonperturbative chiral approach, Phys. Rev. D **59**, 074001 (1999); Erratum, Phys. Rev. D **60**, 099906 (1999); Erratum, Phys. Rev. D **75**, 099903 (2007).

[28] J. A. Oller and E. Oset, N/D description of two meson amplitudes and chiral symmetry, Phys. Rev. D **60**, 074023 (1999).

[29] D. Black, A. H. Fariborz, F. Sannino, and J. Schechter, Evidence for a scalar $\kappa(900)$ resonance in πK scattering, Phys. Rev. D **58**, 054012 (1998).

[30] A. Roessl, Pion kaon scattering near the threshold in chiral SU(2) perturbation theory, Nucl. Phys. **B555**, 507 (1999).

[31] M. Jamin, J. A. Oller, and A. Pich, S wave $K\pi$ scattering in chiral perturbation theory with resonances, Nucl. Phys. **B587**, 331 (2000).

[32] A. Gomez Nicola and J. R. Pelaez, Meson meson scattering within one loop chiral perturbation theory and its unitarization, Phys. Rev. D **65**, 054009 (2002).

[33] J. Bijnens, P. Dhonte, and P. Talavera, πK scattering in three flavor ChPT, J. High Energy Phys. 05 (2004) 036.

[34] J. Nebreda and J. R. Pelaez, Strange and non-strange quark mass dependence of elastic light resonances from SU(3) unitarized chiral perturbation theory to one loop, Phys. Rev. D **81**, 054035 (2010).

[35] Z.-H. Guo and J. A. Oller, Resonances from meson-meson scattering in U(3) CHPT, Phys. Rev. D **84**, 034005 (2011).

[36] P. C. Magalhaes, M. R. Robilotta, K. S. F. F. Guimaraes, T. Frederico, W. de Paula, I. Bediaga, A. C. d. Reis, C. M. Maekawa, and G. R. S. Zarnauskas, Towards three-body unitarity in $D^+ \to K^-\pi^+\pi^+$, Phys. Rev. D **84**, 094001 (2011).

[37] T. Wolkanowski, M. Sołtysiak, and F. Giacosa, $K_0^*(800)$ as a companion pole of $K_0^*(1430)$, Nucl. Phys. **B909**, 418 (2016).

[38] E. van Beveren, T. A. Rijken, K. Metzger, C. Dullemond, G. Rupp, and J. E. Ribeiro, A low lying scalar meson nonet in a unitarized meson model, Z. Phys. C **30**, 615 (1986).

[39] E. van Beveren, D. V. Bugg, F. Kleefeld, and G. Rupp, The nature of σ, κ, $a_0(980)$ and $f_0(980)$, Phys. Lett. B **641**, 265 (2006).

[40] J. R. Pelaez, Light scalars as tetraquarks or two-meson states from large N_c and unitarized chiral perturbation theory, Mod. Phys. Lett. A **19**, 2879 (2004).

[41] T. Ledwig, J. Nieves, A. Pich, E. Ruiz Arriola, and J. Ruiz de Elvira, Large-N_c naturalness in coupled-channel meson-meson scattering, Phys. Rev. D **90**, 114020 (2014).

[42] A. Dobado and J. R. Pelaez, A Global fit of $\pi\pi$ and πK elastic scattering in ChPT with dispersion relations, Phys. Rev. D **47**, 4883 (1993).

[43] A. Dobado and J. R. Pelaez, The Inverse amplitude method in chiral perturbation theory, Phys. Rev. D **56**, 3057 (1997).

[44] P. Buettiker, S. Descotes-Genon, and B. Moussallam, A new analysis of πK scattering from Roy and Steiner type equations, Eur. Phys. J. C **33**, 409 (2004).

[45] S. Descotes-Genon and B. Moussallam, The $K^{*0}(800)$ scalar resonance from Roy-Steiner representations of πK scattering, Eur. Phys. J. C **48**, 553 (2006).

[46] Z. Y. Zhou and H. Q. Zheng, An improved study of the kappa resonance and the non-exotic s wave πK scatterings up to $\sqrt{s} = 2.1$ GeV of LASS data, Nucl. Phys. **A775**, 212 (2006).

[47] J. R. Peláez and A. Rodas, Determination of the Lightest Strange Resonance $K_0^*(700)$ or κ, from a Dispersive Data Analysis, Phys. Rev. Lett. **124**, 172001 (2020).

[48] B. Ananthanarayan and P. Buettiker, Comparison of pion kaon scattering in SU(3) chiral perturbation theory and dispersion relations, Eur. Phys. J. C **19**, 517 (2001).

[49] J. R. Peláez, A. Rodas, and J. Ruiz de Elvira, Strange resonance poles from $K\pi$ scattering below 1.8 GeV, Eur. Phys. J. C **77**, 91 (2017).

[50] J. R. Pelaez and A. Rodas, Pion-kaon scattering amplitude constrained with forward dispersion relations up to 1.6 GeV, Phys. Rev. D **93**, 074025 (2016).

[51] D. V. Bugg, The kappa in E791 data for $D \to K\pi\pi$, Phys. Lett. B **632**, 471 (2006).

[52] D. V. Bugg, The kappa in $J/\psi \to K^+\pi^-K^-\pi^+$, Eur. Phys. J. A **25**, 107 (2005).

[53] E. M. Aitala *et al.* (E791 Collaboration), Dalitz Plot Analysis of the Decay $D^+ \to K^-\pi^+\pi^+$ and the Study of the $K\pi$ Scalar Amplitudes, Phys. Rev. Lett. **89**, 121801 (2002).

[54] J. Z. Bai *et al.* (BES Collaboration), The BES detector, Nucl. Instrum. Methods Phys. Res., Sect. A **344**, 319 (1994).

[55] J. Z. Bai *et al.* (BES Collaboration), The BES upgrade, Nucl. Instrum. Methods Phys. Res., Sect. A **458**, 627 (2001).

[56] M. Lüscher, Two particle states on a torus and their relation to the scattering matrix, Nucl. Phys. **B354**, 531 (1991).

[57] K. Rummukainen and S. A. Gottlieb, Resonance scattering phase shifts on a nonrest frame lattice, Nucl. Phys. **B450**, 397 (1995).

[58] C. h. Kim, C. T. Sachrajda, and S. R. Sharpe, Finite-volume effects for two-hadron states in moving frames, Nucl. Phys. **B727**, 218 (2005).

[59] Z. Davoudi and M. J. Savage, Improving the volume dependence of two-body binding energies calculated with lattice QCD, Phys. Rev. D **84**, 114502 (2011).

[60] Z. Fu, Rummukainen-Gottlieb's formula on two-particle system with different mass, Phys. Rev. D **85**, 014506 (2012).

[61] M. T. Hansen and S. R. Sharpe, Multiple-channel generalization of Lellouch-Lüscher formula, Phys. Rev. D **86**, 016007 (2012).

[62] L. Leskovec and S. Prelovsek, Scattering phase shifts for two particles of different mass and non-zero total momentum in lattice QCD, Phys. Rev. D **85**, 114507 (2012).

[63] M. Gockeler, R. Horsley, M. Lage, U. G. Meissner, P. E. L. Rakow, A. Rusetsky, G. Schierholz, and J. M. Zanotti, Scattering phases for meson and baryon resonances on general moving-frame lattices, Phys. Rev. D **86**, 094513 (2012).

[64] R. A. Briceno, Two-particle multichannel systems in a finite volume with arbitrary spin, Phys. Rev. D **89**, 074507 (2014).

[65] R. A. Briceno, J. J. Dudek, and R. D. Young, Scattering processes and resonances from lattice QCD, Rev. Mod. Phys. **90**, 025001 (2018).

[66] C. Miao, X.-i. Du, G.-w. Meng, and C. Liu, Lattice study on kaon pion scattering length in the $I = 3/2$ channel, Phys. Lett. B **595**, 400 (2004).

[67] S. R. Beane, P. F. Bedaque, T. C. Luu, K. Orginos, E. Pallante, A. Parreno, and M. J. Savage, πK scattering in full QCD with domain-wall valence quarks, Phys. Rev. D **74**, 114503 (2006).

[68] J. M. Flynn and J. Nieves, Elastic s-wave $B\pi$, $D\pi$, DK and $K\pi$ scattering from lattice calculations of scalar form-factors in semileptonic decays, Phys. Rev. D **75**, 074024 (2007).

[69] J. Nagata, S. Muroya, and A. Nakamura, Lattice study of $K\pi$ scattering in $I = 3/2$ and $1/2$, Phys. Rev. C **80**, 045203 (2009); Erratum, Phys. Rev. C **84**, 019904 (2011).

[70] Z.-W. Fu, Lattice calculation of κ meson, Chin. Phys. C **36**, 489 (2012).

[71] Z. Fu, The preliminary lattice QCD calculation of κ meson decay width, J. High Energy Phys. 01 (2012) 017.

[72] Z. Fu, Lattice study on πK scattering with moving wall source, Phys. Rev. D **85**, 074501 (2012).

[73] Z. Fu, Studying κ meson with a MILC fine lattice, Int. J. Mod. Phys. A **28**, 1350059 (2013).

[74] C. B. Lang, L. Leskovec, D. Mohler, and S. Prelovsek, $K\pi$ scattering for isospin $1/2$ and $3/2$ in lattice QCD, Phys. Rev. D **86**, 054508 (2012).

[75] K. Sasaki, N. Ishizuka, M. Oka, and T. Yamazaki (PACS-CS Collaboration), Scattering lengths for two pseudoscalar meson systems, Phys. Rev. D **89**, 054502 (2014).

[76] C. Helmes, C. Jost, B. Knippschild, B. Kostrzewa, L. Liu, F. Pittler, C. Urbach, and M. Werner (ETM Collaboration), Hadron-hadron interactions from $N_f = 2 + 1 + 1$ lattice QCD: $I = 3/2$ πK scattering length, Phys. Rev. D **98**, 114511 (2018).

[77] C. Alexandrou, J. O. Daldrop, M. Dalla Brida, M. Gravina, L. Scorzato, C. Urbach, and M. Wagner, Lattice investigation of the scalar mesons $a_0(980)$ and κ using four-quark operators, J. High Energy Phys. 04 (2013) 137.

[78] S. Prelovsek, T. Draper, C. B. Lang, M. Limmer, K.-F. Liu, N. Mathur, and D. Mohler, Lattice study of light scalar

tetraquarks with I=0,2,1/2,3/2: Are σ and κ tetraquarks? Phys. Rev. D **82**, 094507 (2010).
[79] F.-K. Guo, L. Liu, U.-G. Meissner, and P. Wang, Tetraquarks, hadronic molecules, meson-meson scattering and disconnected contributions in lattice QCD, Phys. Rev. D **88**, 074506 (2013).
[80] M. Doring and U. G. Meissner, Finite volume effects in pion-kaon scattering and reconstruction of the $\kappa(800)$ resonance, J. High Energy Phys. 01 (2012) 009.
[81] V. Bernard, M. Lage, U. G. Meissner, and A. Rusetsky, Scalar mesons in a finite volume, J. High Energy Phys. 01 (2011) 019.
[82] M. Doring, U. G. Meissner, E. Oset, and A. Rusetsky, Scalar mesons moving in a finite volume and the role of partial wave mixing, Eur. Phys. J. A **48**, 114 (2012).
[83] C. W. Xiao, F. Aceti, and M. Bayar, The small $K\pi$ component in the K^* wave functions, Eur. Phys. J. A **49**, 22 (2013).
[84] M. Döring, U.-G. Meißner, and W. Wang, Chiral dynamics and S-wave contributions in semileptonic B decays, J. High Energy Phys. 10 (**2013**) 011.
[85] D. Zhou, E.-L. Cui, H.-X. Chen, L.-S. Geng, and L.-H. Zhu, $K\pi$ interaction in finite volume and the K^* resonance, Phys. Rev. D **91**, 094505 (2015).
[86] Z. Fu and K. Fu, Lattice QCD study on $K^*(892)$ meson decay width, Phys. Rev. D **86**, 094507 (2012).
[87] S. Prelovsek, L. Leskovec, C. B. Lang, and D. Mohler, $K\pi$ scattering and the K^* decay width from lattice QCD, Phys. Rev. D **88**, 054508 (2013).
[88] G. S. Bali, S. Collins, A. Cox, G. Donald, M. Göckeler, C. Lang, and A. Schäfer (RQCD Collaboration), ρ and K^* resonances on the lattice at nearly physical quark masses and $N_f = 2$, Phys. Rev. D **93**, 054509 (2016).
[89] D. J. Wilson, J. J. Dudek, R. G. Edwards, and C. E. Thomas, Resonances in coupled $\pi K, \eta K$ scattering from lattice QCD, Phys. Rev. D **91**, 054008 (2015).
[90] J. J. Dudek, R. G. Edwards, C. E. Thomas, and D. J. Wilson (Hadron Spectrum Collaboration), Resonances in Coupled $\pi K - \eta K$ Scattering from Quantum Chromodynamics, Phys. Rev. Lett. **113**, 182001 (2014).
[91] R. Brett, J. Bulava, J. Fallica, A. Hanlon, B. Hörz, and C. Morningstar, Determination of s- and p-wave $I = 1/2$ $K\pi$ scattering amplitudes in $N_{\mathrm{f}} = 2 + 1$ lattice QCD, Nucl. Phys. **B932**, 29 (2018).
[92] D. J. Wilson, R. A. Briceno, J. J. Dudek, R. G. Edwards, and C. E. Thomas, The Quark-Mass Dependence of Elastic πK Scattering from QCD, Phys. Rev. Lett. **123**, 042002 (2019).
[93] R. A. Briceño, M. T. Hansen, and A. Walker-Loud, Multichannel $1 \to 2$ transition amplitudes in a finite volume, Phys. Rev. D **91**, 034501 (2015).
[94] S. U. Chung, J. Brose, R. Hackmann, E. Klempt, S. Spanier, and C. Strassburger, Partial wave analysis in K matrix formalism, Ann. Phys. (Berlin) **507**, 404 (1995).
[95] L. D. Landau and E. M. Lifshits, *Quantum Mechanics*, Vol. 3 of Course of Theoretical Physics (Butterworth-Heinemann, Oxford, 1991).
[96] K. Krane, *Introductory Nuclear Physics* (Wiley, New York, 1988).
[97] D. V. Bugg, Comments on the sigma and kappa, Phys. Lett. B **572**, 1 (2003); Erratum, Phys. Lett. B **595**, 556 (2004).
[98] D. V. Bugg, An update on the kappa, Phys. Rev. D **81**, 014002 (2010).
[99] S. L. Adler, Consistency conditions on the strong interactions implied by a partially conserved axial-vector current. II, Phys. Rev. **139**, B1638 (1965); Phys. Rev. **139**, 152 (1965).
[100] S. L. Adler, Consistency conditions on the strong interactions implied by a partially conserved axial vector current, Phys. Rev. **137**, B1022 (1965); Phys. Rev. **137**, 140 (1964).
[101] L. Bessler and P. T. Davies, Necessary and sufficient conditions for the Adler zero, Phys. Rev. D **9**, 2923 (1974).
[102] F. Von Hippel and C. Quigg, Centrifugal-barrier effects in resonance partial decay widths, shapes, and production amplitudes, Phys. Rev. D **5**, 624 (1972).
[103] J. M. Link *et al.* (FOCUS Collaboration), The $K^-\pi^+$ S-wave from the $D^+ \to K^-\pi^+\pi^+$ decay, Phys. Lett. B **681**, 14 (2009).
[104] E. M. Aitala *et al.* (E791 Collaboration), Model independent measurement of S-wave $K^-\pi^+$ systems using $D^+ \to K\pi\pi$ decays from Fermilab E791, Phys. Rev. D **73**, 032004 (2006); Phys. Rev. D **74**, 059901 (2006).
[105] K. Symanzik, Improved lattice actions for nonlinear sigma model and non-Abelian gauge theory, in *Workshop on Non-perturbative Field Theory and QCD Trieste, Italy, 1982* (World Scientific, Singapore, 1983), Vol. 61, pp. 61–72.
[106] K. Symanzik, Continuum limit and improved action in lattice theories. 1. Principles and ϕ^4 theory, Nucl. Phys. **B226**, 187 (1983).
[107] K. Symanzik, Continuum limit and improved action in lattice theories. 2. O(N) Nonlinear sigma model in perturbation theory, Nucl. Phys. **B226**, 205 (1983).
[108] M. Lüscher and P. Weisz, Computation of the action for on-shell improved lattice gauge theories at weak coupling, Phys. Lett. **158B**, 250 (1985).
[109] K. G. Wilson, Confinement of quarks, Phys. Rev. D **10**, 2445 (1974); Phys. Rev. D **10**, 319 (1974).
[110] B. Sheikholeslami and R. Wohlert, Improved continuum limit lattice action for QCD with Wilson fermions, Nucl. Phys. **B259**, 572 (1985).
[111] C. Morningstar and M. J. Peardon, Analytic smearing of SU(3) link variables in lattice QCD, Phys. Rev. D **69**, 054501 (2004).
[112] C. T. H. Davies, E. Follana, I. D. Kendall, G. P. Lepage, and C. McNeile (HPQCD Collaboration), Precise determination of the lattice spacing in full lattice QCD, Phys. Rev. D **81**, 034506 (2010).
[113] S. Meinel, Bottomonium spectrum at order v^6 from domain-wall lattice QCD: Precise results for hyperfine splittings, Phys. Rev. D **82**, 114502 (2010).
[114] G. P. Lepage, L. Magnea, C. Nakhleh, U. Magnea, and K. Hornbostel, Improved nonrelativistic QCD for heavy quark physics, Phys. Rev. D **46**, 4052 (1992).
[115] S. Güsken, U. Low, K. H. Mutter, R. Sommer, A. Patel, and K. Schilling, Nonsinglet axial vector couplings of the baryon octet in lattice QCD, Phys. Lett. B **227**, 266 (1989).
[116] M. Albanese *et al.* (APE Collaboration), Glueball masses and string tension in lattice QCD, Phys. Lett. B **192**, 163 (1987).

[117] Mildred Dresselhaus, Gene Dresselhaus, and Ado Jorio, *Group Theory: Application to the Physics of Condensed Matter*, 1st ed. (Springer-Verlag, Berlin, 2008).

[118] C. Alexandrou, L. Leskovec, S. Meinel, J. Negele, S. Paul, M. Petschlies, A. Pochinsky, G. Rendon, and S. Syritsyn, P-wave $\pi\pi$ scattering and the ρ resonance from lattice QCD, Phys. Rev. D **96**, 034525 (2017).

[119] C. McNeile and C. Michael (UKQCD Collaboration), Decay width of light quark hybrid meson from the lattice, Phys. Rev. D **73**, 074506 (2006).

[120] M. Lüscher and U. Wolff, How to calculate the elastic scattering matrix in two-dimensional quantum field theories by numerical simulation, Nucl. Phys. **B339**, 222 (1990).

[121] B. Blossier, M. Della Morte, G. von Hippel, T. Mendes, and R. Sommer, On the generalized eigenvalue method for energies and matrix elements in lattice field theory, J. High Energy Phys. 04 (2009) 094.

[122] See Supplemental Material at http://link.aps.org/supplemental/10.1103/PhysRevD.102.114520 for ancillary files with the spectrum results and the amplitude parametrization fit results for each ensemble.

[123] P. Guo, J. Dudek, R. Edwards, and A. P. Szczepaniak, Coupled-channel scattering on a torus, Phys. Rev. D **88**, 014501 (2013).

[124] R. A. Briceno, J. J. Dudek, R. G. Edwards, C. J. Shultz, C. E. Thomas, and D. J. Wilson, The Resonant $\pi^+\gamma \to \pi^+\pi^0$ Amplitude from Quantum Chromodynamics, Phys. Rev. Lett. **115**, 242001 (2015).

[125] C. Alexandrou, L. Leskovec, S. Meinel, J. Negele, S. Paul, M. Petschlies, A. Pochinsky, G. Rendon, and S. Syritsyn, $\pi\gamma \to \pi\pi$ transition and the ρ radiative decay width from lattice QCD, Phys. Rev. D **98**, 074502 (2018).

[126] R. R. Horgan, Z. Liu, S. Meinel, and M. Wingate, Lattice QCD calculation of form factors describing the rare decays $B \to K^*\ell^+\ell^-$ and $B_s \to \phi\ell^+\ell^-$, Phys. Rev. D **89**, 094501 (2014).

[127] J. Towns, T. Cockerill, M. Dahan, I. Foster, K. Gaither, A. Grimshaw, V. Hazlewood, S. Lathrop, D. Lifka, G. D. Peterson, R. Roskies, J. R. Scott, and N. Wilkins-Diehr, XSEDE: Accelerating scientific discovery, Comput. Sci. Eng. **16**, 62 (2014).